Simulação numérica de comunicações óticas subaquáticas

Veridiano Marques
Mestrado Integrado em Engenharia Física
Departamento de Física e Astronomia
2021

Orientador
Luís Pessoa, Professor Auxiliar Convidado, Faculdade de Engenharia
Supervisor
Henrique Salgado, Professor Associado, Faculdade de Engenharia

U.PORTO
FEUP FACULDADE DE ENGENHARIA
UNIVERSIDADE DO PORTO

U.PORTO
FC FACULDADE DE CIÊNCIAS
UNIVERSIDADE DO PORTO

Todas as correções determinadas pelo júri, e só essas, foram efetuadas.

O Presidente do Júri,

Porto, ______/______/_________

UNIVERSIDADE DO PORTO

MASTERS THESIS

Simulação numérica de comunicações óticas subaquáticas

Author:
Veridiano MARQUES

Supervisor:
LuísPESSOA

Co-supervisor:
Henrique SALGADO

A thesis submitted in fulfilment of the requirements for the degree of MSc. Engineering Physics

at the

Faculdade de Ciências da Universidade do Porto e Faculdade de Engenharia da Universidade do Porto
Departamento de Física e Astronomia (FCUP) e Departamento de Engenharia Electrotécnica (FEUP)

October 26, 2021

" "The things you own end up owning you." "

Tyler Durden

UNIVERSIDADE DO PORTO

Abstract

Faculdade de Ciências da Universidade do Porto e Faculdade de Engenharia da Universidade do Porto

Departamento de Física e Astronomia (FCUP) e Departamento de Engenharia Electrotécnica (FEUP)

MSc. Engineering Physics

Simulação numérica de comunicações óticas subaquáticas

by Veridiano MARQUES

This thesis proposes a multiple sensor-lens pair scheme to increase the misalignment tolerance and presents an accurate model of photon propagation based on the Monte Carlo simulation, that includes the photon refraction at the lenses interface and angular misalignment between emitter and receiver. The results show that the ideal divergence of the emitter's beam is around 15º for a 1 metre Tx-Rx distance, increasing to 22º for a shorter distance of 0.5 metres, but being independent of the water turbidity, showing that the geometry of the link is the dominant factor in such short-range links. Additionally, it was concluded that a 7 lenses scheme is approximately 3 times more offset tolerable than a single lens. Rotating the emitter increases the optimal divergence while rotating the plane of sensors decreases it. A successful Random Forest prediction of misalignment of the AUV in relation to a fixed sensor scheme based on the received light power distribution of each lens. The maximum root medium square error obtained was of 6mm for the radial offset prediction and 10 degrees for the angle, which based on the live conditions are considered good results.

UNIVERSIDADE DO PORTO

Resumo

Faculdade de Ciências da Universidade do Porto e Faculdade de Engenharia da Universidade do Porto
Departamento de Física e Astronomia (FCUP) e Departamento de Engenharia Electrotécnica (FEUP)

Mestrado Integrado em Engenharia Física

Simulação numérica de comunicações óticas subaquáticas

por Veridiano MARQUES

Esta tese propõe um esquema de mútiplos pares sensor-lente para melhorar a tolerância ao desalinhamento em comunicações óticas subaquáticas e apresenta um modelo preciso de propagação de fotões baseado em simulações de Monte Carlo, que inclui a refração do fotão na interface das lentes e o desalinhamento angular entre os emissores e receptor. Os resultados mostram que a divergência ideal do feixe do emissor é de cerca de 15º para um 1 metro de distância Tx-Rx, aumentando para 22º para uma distância mais curta de 0,5 metros, mas sendo independente da turbidez da água, mostrando que a geometria da ligação é o factor dominante em ligações de curta distância. Além disso, concluiu-se que um esquema de 7 lentes é aproximadamente 3 vezes mais tolerável ao desalinhamento lateral do que uma única lente. Também que a rotação do emissor aumenta a divergência óptima enquanto a rotação do plano dos sensores faz com que esta diminua. Uma previsão bem sucedida do desalinhamento lateral do AUV em relação a um esquema de sensor fixo foi obtida usando um método Random Forest baseado na distribuição da potência luminosa recebida de cada lente. O erro quadrático médio máximo obtido foi de 6mm para a previsão do desvio radial e de 10 graus para o ângulo, que, com base nas condições de comunicação subaquática reais, são considerados bons resultados.

Contents

Abstract **v**

Resumo **vii**

Contents **ix**

List of Figures **xi**

Glossary **xiii**

1 Introduction **1**
1.1 Contributions 3

2 Overview of the State-of-The Art **5**
2.1 Historic Perspective 5
2.2 Underwater Communication Methods 6
2.2.1 Acoustic Communication 6
2.2.2 Radio Frequency Communication 6
2.3 Underwater Optical Wireless Communications 8
2.3.1 Transmitter (TX) - Receiver (RX) Connection 9
2.3.1.1 Line of Sight (LOS) configuration 9
2.3.1.2 Diffuse (LOS) configuration 9
2.4 Underwater Optical Wireless Channel Modeling 10
2.4.0.1 Beer-Lambert Law 10
2.4.0.2 Summary 11

3 Underwater Light Propagation **13**
3.1 Inherent Optical Properties (IOP) 13
3.2 Absorption 15
3.3 Scattering 18
3.4 Measured Water Parameters 19
3.4.1 Measured Scattering Phase Functions 19
3.4.2 Analytical Phase Functions 20
3.4.3 Radiative Transfer Equation 21

4 Monte Carlo Photon Propagation Algorithm **23**
4.1 Assumptions and Approximations 23

4.2 The Algorithm . . . 24
4.2.1 Coordinate System . . . 24
4.2.1.1 Emitter and Photon Initial Conditions . . . 25
4.2.2 Photon Propagation . . . 27
4.2.3 Absorption - Photon Weight and types of Monte Carlo Algorithm . . . 28
4.2.4 Scattering . . . 28
4.3 Validation of Simulation Model . . . 29
4.4 Emitter and Sensor Rotation . . . 30
4.5 Sensor Architecture . . . 33
4.5.1 Accurate Lens Behaviour . . . 33
4.5.2 Packing . . . 33

5 Prediction and Optimization Techniques used **37**
5.1 Particle Swarm Optimization . . . 37
5.2 Decision Tree and Random Forest Learning . . . 38
5.2.1 Decision Tree . . . 38
5.2.2 Random Forest . . . 39

6 Results **41**
6.1 General Simulation Parameters . . . 41
6.2 Equivalence of Monte Carlo Methods . . . 41
6.3 Link Misalignment analysis . . . 42
6.3.1 Offset Misalignment Results . . . 44
6.3.1.1 Types of Water . . . 44
6.3.1.2 Propagation Distance . . . 44
6.3.1.3 Sensor Scheme . . . 45
6.3.1.4 Rotation Misalignment . . . 46
6.4 Lens Scheme Optimization . . . 49
6.5 Live Misalignment Offset Prediction . . . 50

7 Conclusion and Future Work **55**

myrefs$_{new}$ **57**

List of Figures

1.1 Transmission window for UOWC [4] 2
1.2 Typical Applications of UOWC [4] 3

2.1 RF attenuation in sea water [11] 7
2.2 RF attenuation in sea water [13] 8
2.3 Point-to-point LOS configuration [27] 9
2.4 Diffuse LOS configuration [27] 10

3.1 Geometry of the inherent optical properties of water 14
3.2 Absorption spectra of pure seawater [32]. 15
3.3 Absorption spectra of CDOM [32]. 16
3.4 Absorption spectra of phytoplankton [32] 16
3.5 Absorption spectra of detritus [32]. 17
3.6 Log-log plots of Petzold's measured volume scattering functions from three different waters, as labeled. [33] 20
3.7 Log-linear plots of Petzold's measured volume scattering functions from three different waters, as labeled. [33] 20
3.8 Comparison of the particulate phase functions with the Petzold's average particle phase function (reference) in a semi-log plot. [34] 21

4.1 Flowchart of the Photon Propagation Algorithm [35] 24
4.2 Scheme of the opening of the optical beam passing it through a lens. 26
4.3 Illustration of direction cosines. The blue vector represents the photon's direction vector,the red vectors, (μ_x, μ_y, μ_z), are the projections of the photon's direction vector onto the x,y and z axis. axes. 26
4.4 Photon propagation illustrated. Each scattering event changes the photon's trajectory and therefore it's θ, ϕ, [35]. 29
4.5 Validation of results - Comparison with Cox's experimental data of a 3.6m water tank with different attenuation coefficients made by adding different quantities of scattering agent Malox. 30
4.6 Rotation of the emitter direction. From the default $\hat{\mathbf{z}}$ direction to any desired vector ω 31
4.7 AUV communicating with fixed receiver. Both emitter and receiver have the same radial direction ϕ but are rotated in relation to the z-axis, by the angles γ_e and γ_s respectively. 32
4.8 Photon as ray vector being refracted at both medium interfaces. The lens directs the photons to the sensor. 34
4.9 Scheme of N sensors given by "circles inside circle" packing algorithm. (a) N=7; (b) N=6; (c) N=5; (d) N=4. 35

5.1 Particle Swarm Optimization . . . 38
5.2 Regression Tree for Medium Home Value . . . 39
5.3 Random Forest Structure . . . 40

6.1 Comparison of the Monte Carlo methods . . . 42
6.2 Moving scheme of sensors for MARO calculation. The sensor scheme is offset through the 2D plane radially from 0 m to 0.4 m and in angle from 0 to 360 degrees in steps of 45 degrees. . . . 43
6.3 MARO calculation as a function of the emitter's divergence for different water types. Tx-Rx distance of 1 metre, 7 lenses scheme. . . . 44
6.4 MARO calculation for different water types at different Tx-Rx distances, N=7 lenses scheme. . . . 45
6.5 MARO calculation as a function of the emitter's divergence for different number of sensors on the sensor scheme. Clear waters and Tx-Rx distance of 1 m. . . . 46
6.6 MARO calculation as a function of the emitter's divergence for rotated communication links. Harbor II waters and Tx-Rx distance of 0.5 metres, N=7 lenses scheme. . . . 47
6.7 Maximum MARO (a) and Divergence for max. MARO (b) and as function of the rotation angle. Harbor II waters and Tx-Rx distance of 0.5 metres, N=7 lenses scheme. . . . 48
6.8 7 lenses scheme with external variable external radius . . . 49
6.9 AUV communicating with fixed receiver using a divergent optical beam. . . 50
6.10 Visual comparison of the predicted radius and the real value - 0.5m . . . 51
6.11 Visual comparison of the predicted angle θ and the real value - 0.5m . . . 52
6.12 Visual comparison of the predicted radius and the real value - 1m . . . 52
6.13 Visual comparison of the predicted angle θ and the real value - 1m . . . 53

Glossary

QM	Quantum Mechanics
UWOC	Underwater Wireless Optical Communications
AUV	Autonomous Underwater Vehicle
ROV	Remotely Operated Vehicles
LED	Light Emitting Diode
Gbps	Gigabits per second
LD	Laser Diode
LOS	Line of Sight
QED	Quantum Electrodynamics
IOP	Inherent Optical Properties
AOP	Apparent Optical Properties
RTE	Radiative Transfer Equation
AW	Albedo-weight method
AR	Albedo-rejection method
PMT	Photomultiplier tube
BER	Bit Error Rate
MALO	Maximum allowed lateral offset
MARO	Maximum allowed radial offset
PSO	Particle swarm optimization

Without a doubt, I dedicate this master thesis to my parents. All their support and love throughout my life has been fundamental to get this far.

A special thanks to:

Prof. Luís Pessoa, for believing in me, for the constant friendly contact, the motivation and for suggesting this project two years ago.

Prof. Henrique Salgado, for all the wise insights and clear explanations during this work.

Prof. João Viana Lopes, for introducing me to the world of physics simulations and being a life mentor.

To my friends, Catarina, Diogo and Joana, for the long-lasting friendship.

And to Valentina, for all the emotional help and insistence to write this on time.

Veridiano Marques

Chapter 1

Introduction

It's widely accepted that *Underwater Wireless Optical Communications* (UWOC) are the future of underwater short-range communications. To the day, UWOC is already employed in several distinct applications as monitoring of mineral sites, communications between submarines and *Autonomous Underwater Vehicles* (AUV's) and even between divers and fixed underwater platforms. Other applications also include ocean data sampling and marine archaeology with live video transmission. An excellent underwater communication system for monitoring and sensing the ocean has a tremendous scientific, industrial and even military interest. In addition, due to global warming, constantly monitoring water levels, quality, and marine life has led to new research in underwater communication methods [1]. The scarcity and progressive shortage of mineral and energetic resources on land have also empowered the underwater mining field and subsequent (UWOC) development for *remotely operated vehicles* (ROV). However, the existing technologies don't match the future needs, RF frequencies have a short propagation distance, and acoustic communication systems have low data rates [2]. This lack leaves UWOC as a viable alternative for low-latency, high data rate communication. Engineers naturally take advantage of the "blue/green" optical window of low absorption and low chromatic dispersion in ocean water. In addition, underwater optical communication systems can be built with low-cost optical sources, like diode lasers or *Light Emitting Diodes* (LED's) [3].

Despite its attractiveness, the optical channel has diverse factors such as environmental conditions, temperature fluctuations, scattering and dispersion, that affect its performance. Allied with the fact that live testing of all the components is expensive, numerical

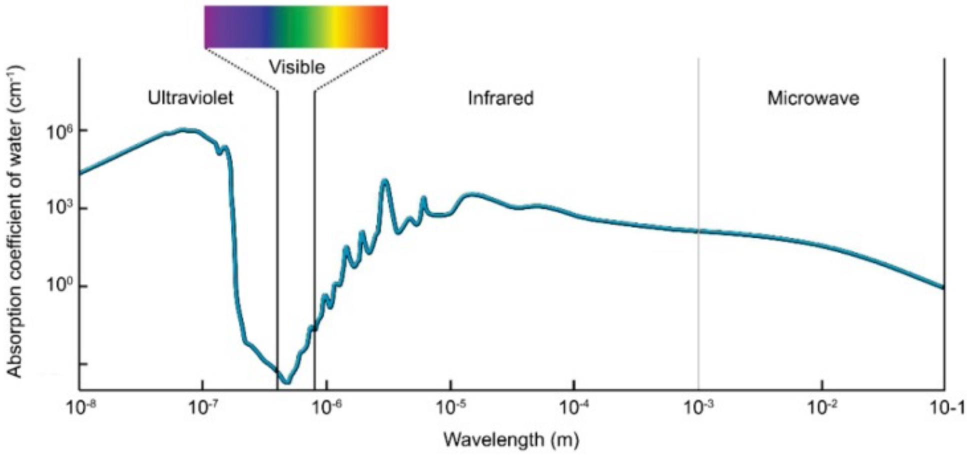

FIGURE 1.1: Transmission window for UOWC [4]

simulations are an alternative to better study what is happening. A vital tool to simulate the underwater optical channel behaviour is a Monte Carlo method that simulates the propagation of photons underwater. This method is widely recognised as an accurate one.

This master thesis research aims to test and evaluate the performance of a different number of scenarios while improving and adding new features to already existing Monte Carlo photon propagating code.

The following chapters will walk thorough the current state of the art of underwater optical communications. After that, a detailed explanation of the physical interactions of light and water in the ocean. Third, a brief explanation of the simulation code, a detailed explanation of the new features added, and validation of the simulation results. Finally several communication scenarios are simulated. Some analysis of system limitations that permit communications engineers to built their systems more efficiently are shown.

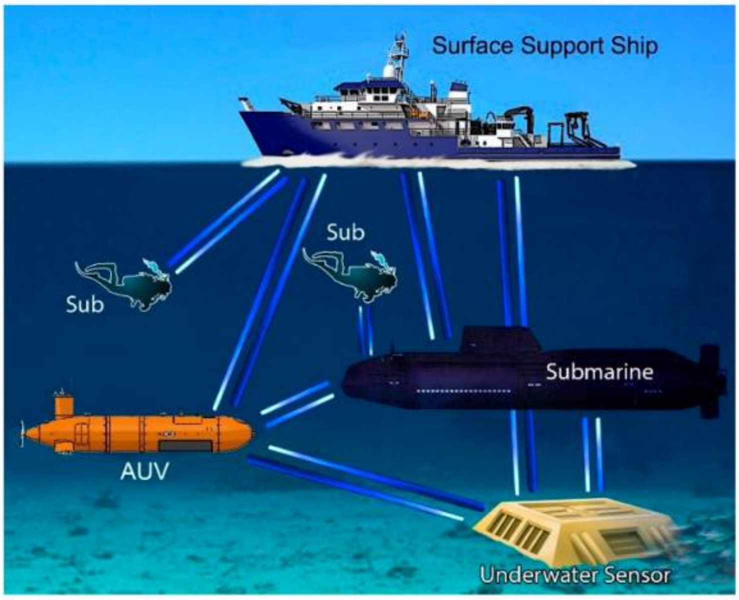

FIGURE 1.2: Typical Applications of UOWC [4]

1.1 Contributions

This thesis contributes to the area of optical communications, specially underwater communications, by adding several new features to the already existing simulation codes such as the ability to have a divergence in the emitter's beam, a rotation of the emitter direction and the plane of sensors, an accurate physical model of the reception lenses and an optimal sensor scheme distribution. Results found on this thesis of the limitations of each communication scenario serve as a guiding map for engineers that want to build optimal systems, by optimizing parameters such as the power or the divergence of the emitter needed in each scenario.

Specific results from this thesis were presented at IEEE International Symposium on Personal, Indoor and Mobile Radio Communications 2021 with an article named: "Modelling of an Underwater Optical Wireless Communication System With Misalignment Tolerance". This article will be published at IEEE Xplore®.

Chapter 2

Overview of the State-of-The Art

2.1 Historic Perspective

The transmission of optical signal transmission starts with Ancient Greek and Roman soldiers that used their polished shields to reflect sunlight to signal long distances. This is considered the first heliograph. [5]. An heliograph is semaphore system that sends signals by transmitting flashes of sunlight, modulation is achieved by pivoting a mirror or interrupting its beam with a shutter. The communication protocol was normally Morse code [6]. The first description of a heliograph is from 1292 but only on the 1810 Karl Gauss built and documented one rigorously. Optical telegraph systems were widely used across the 19 century. A lot of telegraph hills can still be found around the world. The invention of the laser in the 1960 by Gordon Gould gave an impulse in the field of free space optical communications. Some years later around 1980s, a lot of military interest in laser free-space communications between submarines grew [7] [8]. By the end of the Cold War, the reduced need in this type of technologies and a increase in the need for terrestrial communications directed research to fiber optics and infrared detectors. The recent increasing interest in ocean monitoring due to climate change and pure ocean observation aligned with the fast proliferation of AUV's started a resurgence of the research interest in underwater optical communication systems.

2.2 Underwater Communication Methods

2.2.1 Acoustic Communication

Acoustic waves are produced from variations of pressure in a medium. Acoustic waves are in general selected as the default primary carrier for underwater wireless among the other possible waves, either RF or optical. This preference is due to have lower absorption and longer coverage distance. Their velocity is of 1500 m/s approximately which leads to large latency over long communication distance. As an example, in, the system data rates degrades from 20Kbps for a 1km distance in deep ocean, to 300 - 500 bps for distance of 100 km in shallow water and 200km in deep ocean [9]. Acoustic communication suffers from multipath propagation due to reflections from the water surface interface and the seafloor, and refractions from the varying sound speed. The typical motion between the transmitter and receiver that happens in underwater scenarios due to currents affect severely this type of communication due to the resultant large Doppler shift [10]. The maximum bandwidth achieved by acoustic waves is on the hundreds of Khz which is not sufficient to video transmissions.

2.2.2 Radio Frequency Communication

Radio frequency waves are electromagnetic waves in the frequency band below 300 GHz. The propagation of RF waves underwater differs from spacial RF waves because of the high water electrical conductivity at high frequency. For high frequencies the attenuation of RF is increasingly higher.

The absorption coefficient on sea water is given by [11]:

$$a_{seawater} \approx \sqrt{\pi f \mu \sigma} \tag{2.1}$$

where α is the absorption coefficient, f the operating frequency, μ the permeability of the medium and σ its conductivity.

Curiously on fresh water this parameter is nearly frequency independent:

$$a_{freshwater} \approx \frac{\sigma}{2}\sqrt{\frac{\mu}{\varepsilon}} \tag{2.2}$$

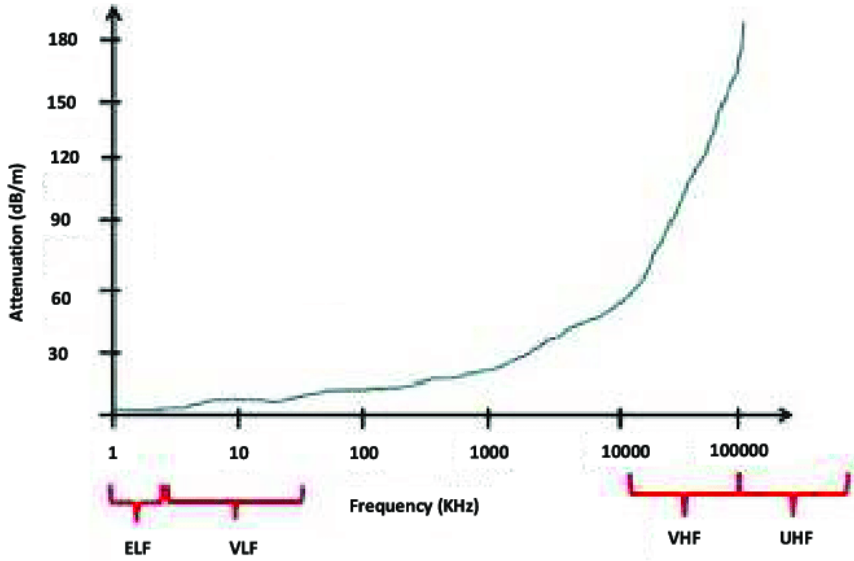

FIGURE 2.1: RF attenuation in sea water [11]

Here ϵ is the permittivity. Although it looks promising to fresh waters, RF still needs antennas with very large size and high transmission power to compensate for the high antenna losses.

2.3 Underwater Optical Wireless Communications

Underwater optical wireless communications surge as an alternative of the technologies above described. They can achieve data rates of Gbps on a smaller distance of up to a potential 500m. To take advantage of the minimum of the absorption coefficient of water, typical transmitter sources have a wavelength between 400 nm-550nm. These light sources are either Laser Diodes (LDs) or LEDs. LDs have higher modulation bandwidth but are also more expensive. For medium bit rate applications LEDs are usually chosen for their higher power efficiency, lower cost and longer lifetime [12].

Table 2.1 summarizes a performance comparison between the three principal underwater communication technologies: acoustic, radio frequency and optical [13].

TABLE 2.1: Comparison of underwater wireless communication technologies [13]

Parameter	Acoustic	RF	Optical
Attenuation	Distance and frequency dependent (0.1–4 dB/km)	Frequency and conductivity dependent (3.5–5 dB/m)	0.39 dB/m (ocean) 11 dB/m (turbid)
Speed	1500 ms^{-1}	2.3×10^8 ms^{-1}	2.3×10^8 ms^{-1}
Data Rate	kbps	Mbps	Gbps
Latency	High	Moderate	Low
Distance	more than 100 km	≤10 m	10–150 m (500 m potential)
Bandwidth	1 kHz–100 kHz	MHz	150 MHz
Frequency Band	10–15 kHz	30–300 MHz	5×10^{14} Hz
Transmission Power	10 W	mW–W	mW–W

A typical UWOC system is composed of a transmitter, a water channel and a receiver. A typical schematic figure can be seen on 2.2. The Transmitter is composed of a modulator and a pulse shape circuit, a driver that converts the electrical signal to an optical one and an output lens. The receiver is composed by a symmetric system, an optical bandpass filter, a lens that collects the photons, a photodetector, an amplifier and a demodulator.

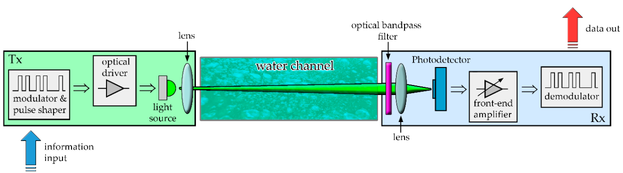

FIGURE 2.2: RF attenuation in sea water [13]

The latest results found on literature for highest data rate achieved by underwater optical communications are summarized on Table 2.2.

TABLE 2.2: State-of-the-art work in UOWC [14]

Data Rate	Light source	Distance	Modulation
2.8 Mbps [15]	470 nm LED	50 m	DPIM
800/200 Mbps [16]	440 nm μLED	0.6/5.4 m	OOK-NRZ
4.8 Gbps [17]	450nm LD	5.4 m	OFDM
5.2/12.4 Gbps [18]	450 nm LD	10.2/1.7 m	OFDM
5 Gbps [19]	450 nm LD	50 m	DFT-S DMT
1.5 Gbps [20]	450 nm LD	20 m	OOK-NRZ
2.7 Gbps [21]	450 nm LD	34.5 m	OOK-NRZ
9.6 Gbps [22]	520 nm LD	8 m	OFDM
12.64 Gbps [23]	405 nm LD	35 m	PS-OFDM
16.6 Gbps [24]	450 nm LD	5 m	DMT
30 Gbps [25]	488 nm LD	12.5 m	4-PAM
12.288 Mbps [26]	460 nm LED	2 m	4-PAM-OOK

2.3.1 Transmitter (TX) - Receiver (RX) Connection

There's two type of communications between transmitter and receiver: diffuse line of sight (diffuse LOS) configuration and point-to-point line-of-sight (LOS) configuration.

2.3.1.1 Line of Sight (LOS) configuration

Line of Sight point to point is the most common configuration in UWOC. The emitter and the receptor must be aligned. This alignment is the limiting factor in respect to this type of communication due to the narrow laser beam width's used. High turbidity and non stationary communication elements caused by tides and waves accentuate even more the problem.

FIGURE 2.3: Point-to-point LOS configuration [27]

2.3.1.2 Diffuse (LOS) configuration

Diffuse emitter light can be achieved by using light emitting diodes (LEDs) that have a higher divergence than lasers or emission systems composed by a laser and a expanding lens in front of it. Diffuse LOS communication reduces the data rate due to higher scattering occurred and the own spread of power caused by the emitter's divergence. On the other hand, improves the tolerance of the communication to unwanted changes in the position of elements that break the alignment. It's mainly used for communicating with several nodes.

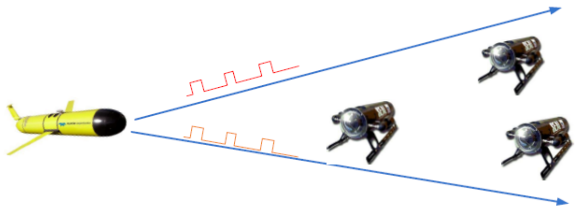

FIGURE 2.4: Diffuse LOS configuration [27]

2.4 Underwater Optical Wireless Channel Modeling

In order to derive channel models and to predict the behaviour of a light beam underwater, it's first necessary to understand the interaction of light with matter. This interaction is only exactly described by particle physics specifically by *quantum electrodynamics* (QED). Quantum electrodynamics is a relativistic quantum field theory, it describes the quantization of the electromagnetic field as an ensemble of harmonic oscillators and introduces the concept of creation and annihilation operators of particles. The problem with this theory is that first is probabilistic and second that can only be solved explicitly for simple particle interactions it gives extremely accurate predictions of quantities like the anomalous magnetic moment of the electron and the Lamb shift of the energy levels of hydrogen [28]. Not ideal for an underwater channel, where multiple light matter interactions occur simultaneously.

2.4.0.1 Beer-Lambert Law

A first calculated guess to determine the loss of light along a path length r is the Beer Lambert Law, also known as Beer's Law [29]. It's the simplest and the most widely used model to describe light attenuation effects underwater. Since the attenuation coefficient c has units m^{-1}, we can calculate a differential intensity loss dI over a differential length dr by:

$$dI = -cIdr \tag{2.3}$$

Where I is the incident power on the volume of width dI, Rearranging this equation and integrating yelds:

$$\int_{I_0}^{I} \frac{1}{I} dI = -c \int_{0}^{r} dr \Rightarrow \ln(I) - \ln(I_0) = -cr \tag{2.4}$$

The final expression for light intensity along the propagation axis is the:

$$I = I_0 \exp(-cr) \tag{2.5}$$

This equation always overestimates loss because assumes that all scattered light is lost from the beam. It also assumes a receiver of infinite aperture.

2.4.0.2 Summary

In order to go around QED, some Monte Carlo Methods have had a lot of research in the last years. The Monte Carlo photon propagation algorithm is a widely documented method to simulate UWOC. Its popularity comes from its simplicity to solve the photon propagation problem against the more accurate but tremendously more complex direct solution of the *Radiative Transfer Equation* (RTE) [30]. Instead of solving the RTE explicitly, Monte Carlo Methods solve it numerically. This function will be presented in the next chapter after the proper introduction to water proprieties. It is also more accurate than the Beer-Lambert law, which is often employed to analyze the absorption losses through propagation [29]. This Monte Carlo algorithm is a statistical method that mimics the behaviour of individual photons through the water. Basically, photons are treated as particles that move through the medium with a given photon path length between events. An event can be absorption or a collision with particles suspended in the water. Two distinct probability density functions give the photon path length between events and the scattering angle after a given collision. Each photon has a given amplitude starting as one, and each time it is absorbed, its amplitude is multiplied by the water albedo coefficient.

Chapter 3

Underwater Light Propagation

3.1 Inherent Optical Properties (IOP)

As introduced in 2.4 Monte Carlo algorithms, used for modeling light behaviour on a water channel, consider only two possible final outcomes for a photon-matter interaction: photon absorption and photon scattering. The probability/intensity of absorption or scattering phenomena will be determined by optical properties of water. Mobley in [31], defined two classes of optical properties, *Inherent optical properties* (IOPs) and *Apparent optical properties* (AOPs). AOPs depend on the propagation medium and on the geometric structure of the ambient light field, whereas IOPs only depend on the medium. For our interests, in this thesis, only IOPs will be described.

If we consider a differential unit of volume of water with width Δr and infinitesimal height and length, the amount of light leaving the volume equals the amount of light entering the volume less any absorption loss in the volume. Due to scattering some amount of light will be scattered into other directions.

Defining the spectral radiant incident power as ϕ_i, the absorbed power as ϕ_a and the total scattered power in all directions as ϕ_s. The incident spectral radiant power as units of Wnm^{-1} and is calculated as:

$$\phi_i(\lambda) = \frac{hc}{\lambda}\frac{N}{\Delta\lambda} \tag{3.1}$$

Where $\frac{hc}{\lambda}$ is the energy of each photon with wavelength λ, $\Delta\lambda$ is the window of wavelength used and N the number of photons observed per second. Defining the absorptance as:

$$A(\lambda) = \frac{\phi_a}{\phi_i} \tag{3.2}$$

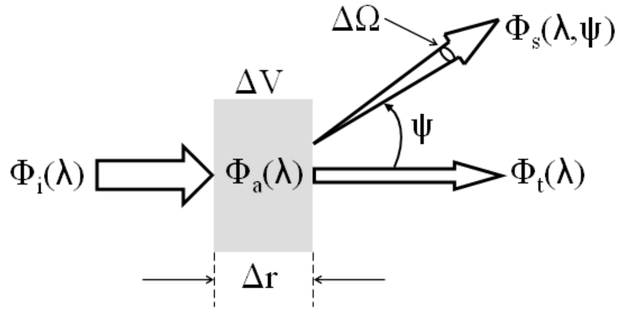

FIGURE 3.1: Geometry of the inherent optical properties of water

the transmittance as:

$$T(\lambda) = \frac{\phi_t}{\phi_i} \tag{3.3}$$

and a scattered power ratio as:

$$B(\lambda) = \frac{\phi_s}{\phi_i} \tag{3.4}$$

Diving all the above quantities by a distance Δr which approaches the infinitesimal limit dr, the above quantities become coefficients which measure loss per unit distance: absorption coefficient:

$$a(\lambda) = \frac{dA(\lambda)}{dr} \tag{3.5}$$

scattering coefficient

$$b(\lambda) = \frac{dB(\lambda)}{dr} \tag{3.6}$$

These have units of m^{-1}. The total loss is defined as the attenuation coefficient, c:

$$c = a + b \tag{3.7}$$

A very interesting and helpfull future value is the single scattering albedo, ω_0,

$$\omega_0 = \frac{b}{c} \tag{3.8}$$

This variable is defined as the ration of scattering loss to total loss. A completely scattering medium would have a value of 1, while a medium with no scattering and only absorption loss would have a value of 0. It will be a decision factor later, to chose whether a photon is going to be absorbed or scattered.

3.2 Absorption

When a photon is absorbed, it's lost permanently. Due to the different constituents of the ocean water, which each have a absorption spectrum. The total absorption spectrum of water is normally represented as a sum of each constituent's absorption coefficient:

$$a(\lambda) = a_{\omega}(\lambda) + a_{CDOM}(\lambda) + a_{phy}(\lambda) + a_{det}(\lambda) \tag{3.9}$$

Where $a_{\omega}(\lambda)$ is the absorption due to pure seawater, $a_{CDOM}(\lambda)$ the absorption due to CDOM, also represented as gelbstoff, yellow substances or gilvin, $a_{phy}(\lambda)$ denotes the absorption due to phytoplankton and $a_{det}(\lambda)$ the absorption due to detritus [32].

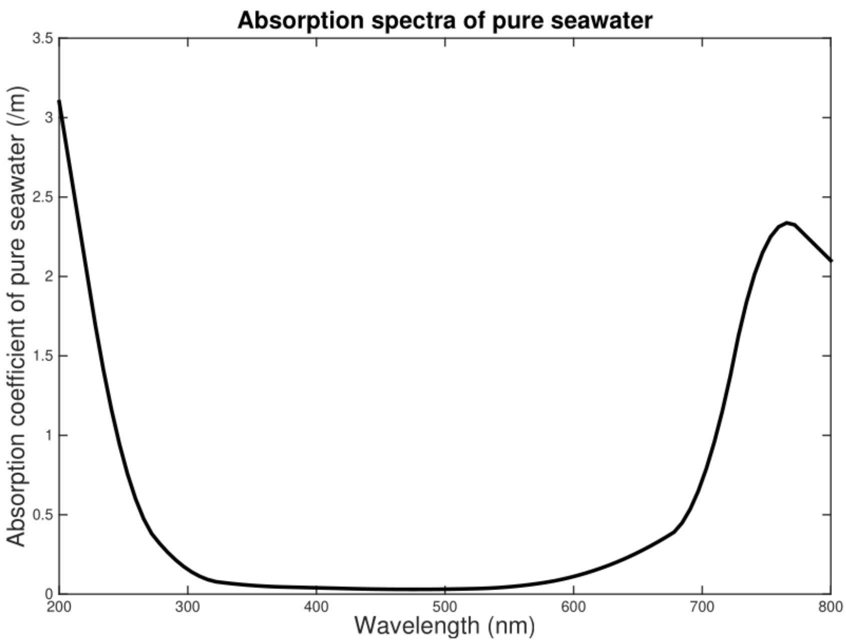

FIGURE 3.2: Absorption spectra of pure seawater [32].

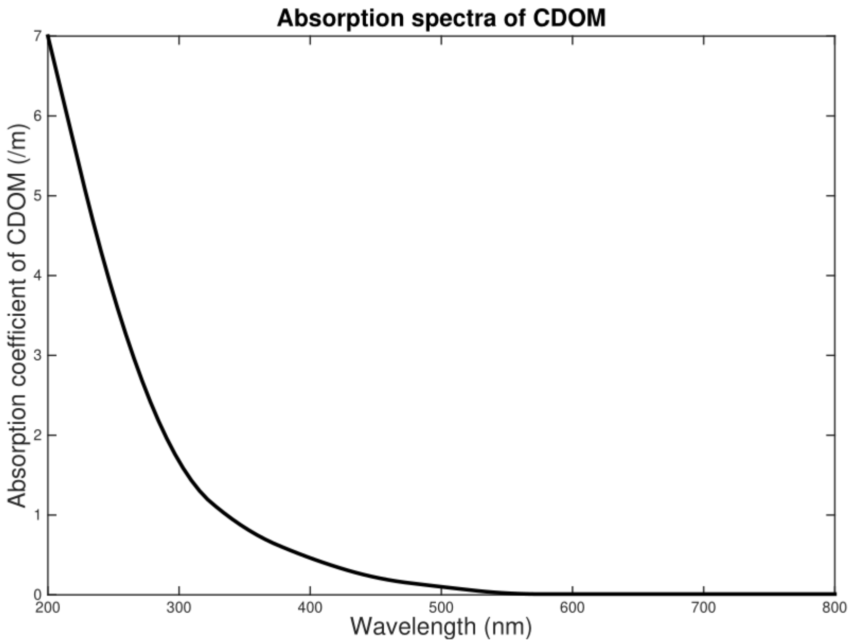

FIGURE 3.3: Absorption spectra of CDOM [32].

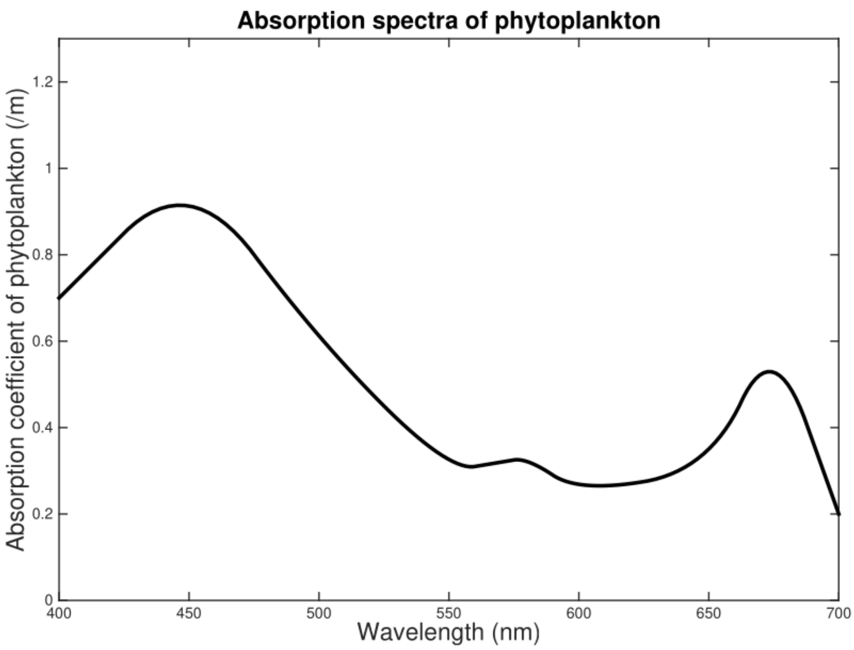

FIGURE 3.4: Absorption spectra of phytoplankton [32]

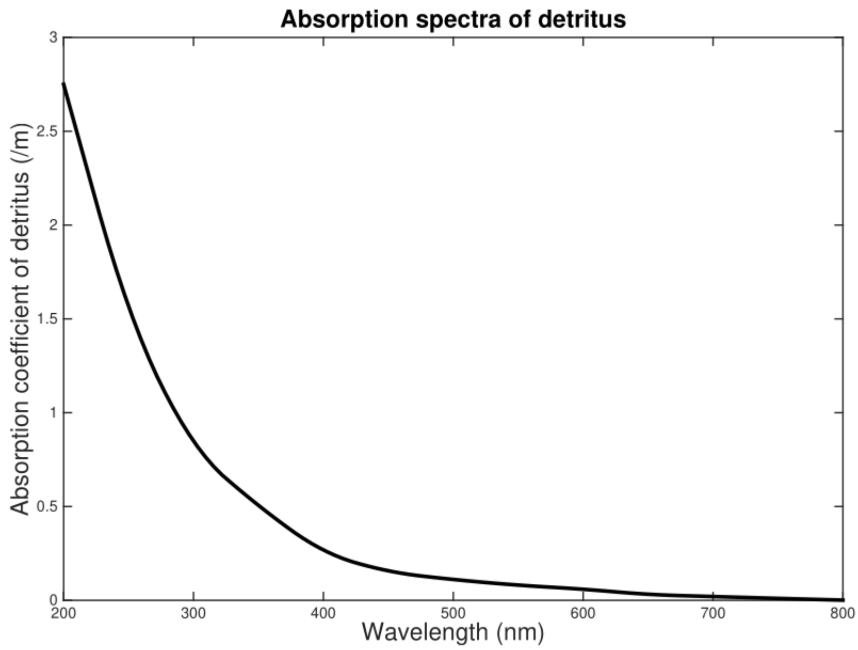

FIGURE 3.5: Absorption spectra of detritus [32].

3.3 Scattering

Scattering can be simply defined as the dispersion of incident photons into other directions. This phenomenon happens due to collisions of photons with particles in the medium which change the photons initial momentum direction. An angular redistribution of the optical field results in losing light intensity in the forward direction. In coastal water scattering is principally due to inorganic matter while in the open ocean is due to organic particles such as phytoplankton. There's three regimes of scattering based on the size of the particles [31]:

- molecular (Rayleigh) scattering, happens when particles radius much lower than λ. Caused by inhomogeneous local concentrations of molecules and particulate matter and other dissolved substances in the water. It has an intensity proportional to the sixth power of the particles diameter and inversely proportional to the fourth power of the light wavelength.
- turbulent scattering, dominant when particles have radius approximately the same size as λ. Intensity proportional to the square of the particle diameter. It's not dependant on the light wavelength but it has very large fluctuations with temperature.
- large particles, with sizes ten times λ.

The intensity of the beam loss from scattering, ϕ_s, is dependent on the angle ψ, this angles measures the deviation from the original incident beam. The angular distribution of scattering, called the volume scattering function, is defined taking the limit of light scattering out of the volume Δr into the solid angle $\Delta\Omega$ in direction ψ, as both tend to zero.

$$\beta(\lambda,\psi) = \lim_{\Delta r\to 0}\lim_{\Delta\Omega\to 0}\frac{\phi_s(\psi;\lambda)}{\phi_i(\lambda)\Delta r\Delta\Omega} \tag{3.10}$$

The units of $\beta(\lambda;\psi)$ are $m^{-1}sr^{-1}$. An expression for $b(\lambda)$ is obtained by integrating β over all angles:

$$b(\lambda) = \int_{4\pi}\beta(\psi;\lambda)d\Omega = 2\pi\int_0^{\pi}\beta(\psi;\lambda)\sin\psi d\psi \tag{3.11}$$

By normalizing the volume scattering phase function, β, by the scattering coefficient, b, one obtains the volume scattering phase function, $\widetilde{\beta}$, which is a *probability density function* (PDF) of the angle of deviation obtained due to scattering.

$$\widetilde{\beta}(\lambda, \psi) = \frac{\beta(\lambda; \psi)}{b(\lambda)} \tag{3.12}$$

The normalization equation condition consequent from combining 3.11 and 3.12 is:

$$2\pi \int_{0}^{\pi} \widetilde{\beta}(\theta, \lambda) \sin(\theta) d\theta = 1 \tag{3.13}$$

By averaging the cosine of the scattering angle, θ over all scattering directions, one obtains the mean cosine, g:

$$g{=}2\pi \int_{0}^{\pi} \widetilde{\beta}(\theta) \cos(\theta) \sin(\theta) d\theta \tag{3.14}$$

This value, g, will be near one for very large phase function values corresponding to small scattering angles.

3.4 Measured Water Parameters

There are several characterizations of water types, in this work the following types of water were considered with the following parameters. To note that the attenuation coefficient and the single scattering albedo are sufficient to calculate the other water parameters, absorption coefficient and scattering coefficient.

TABLE 3.1: Measured parameters for different water types [31]

Water Type	$c(\lambda)$	ω_0
Clear Waters	$0.15m^{-1}$	0.25
Coastal Waters	$0.4m^{-1}$	0.55
Harbor I Waters	$1.1m^{-1}$	0.83
Harbor II Waters	$2.19m^{-1}$	0.83

3.4.1 Measured Scattering Phase Functions

The reference for every modeling of the scattering phase function is Petzold's Measurements, which are the most carefully made scattering measurements on literature. He combined two measures of angles with two different measurements, one for small angles and other for angles between 10 and 170 degrees. The very clear water are taken on the Bahamas, coastal on California and turbid harbor on San Diego.

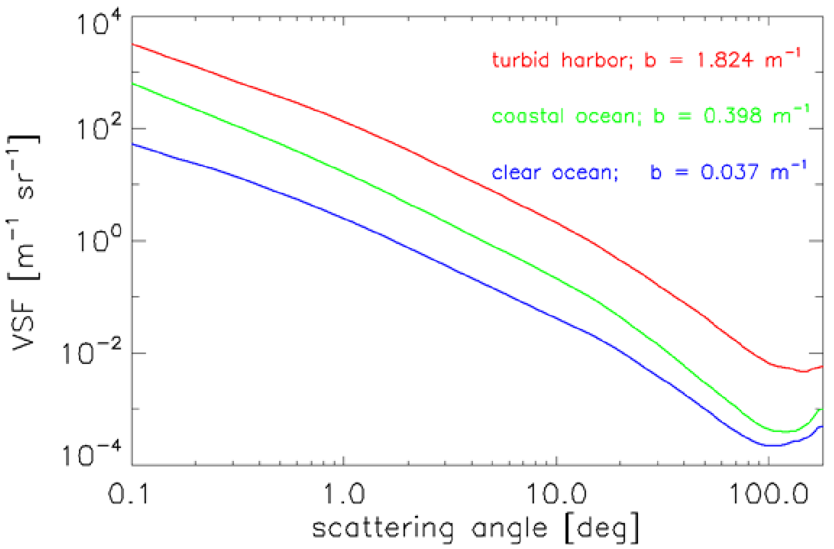

FIGURE 3.6: Log-log plots of Petzold's measured volume scattering functions from three different waters, as labeled. [33]

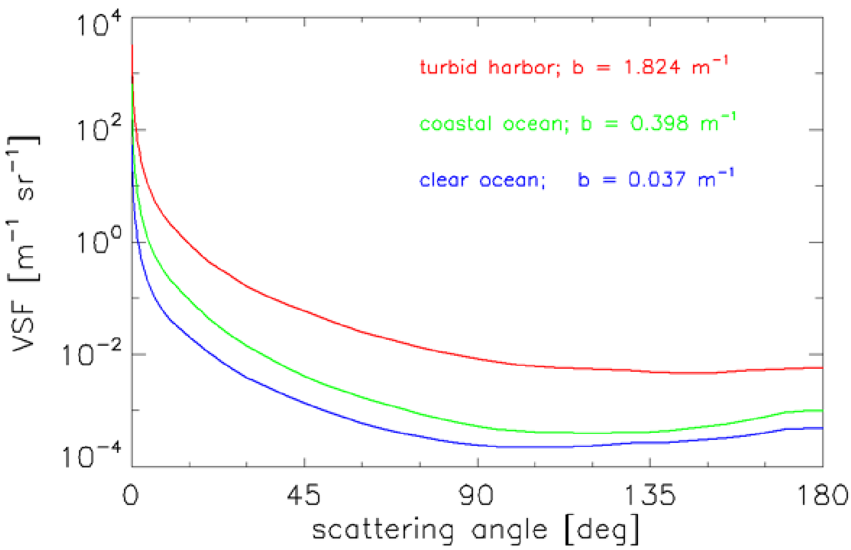

FIGURE 3.7: Log-linear plots of Petzold's measured volume scattering functions from three different waters, as labeled. [33]

3.4.2 Analytical Phase Functions

Several analytical attempts to model accurately the scattering phase function have been made. To this day, to the best of the author's knowledge the one that better agrees with Pezthold results is the: Sahu and Shanmugan phase function with flat back approximation [34].

The equations and the parameters required to the equations are all very well described in [34].

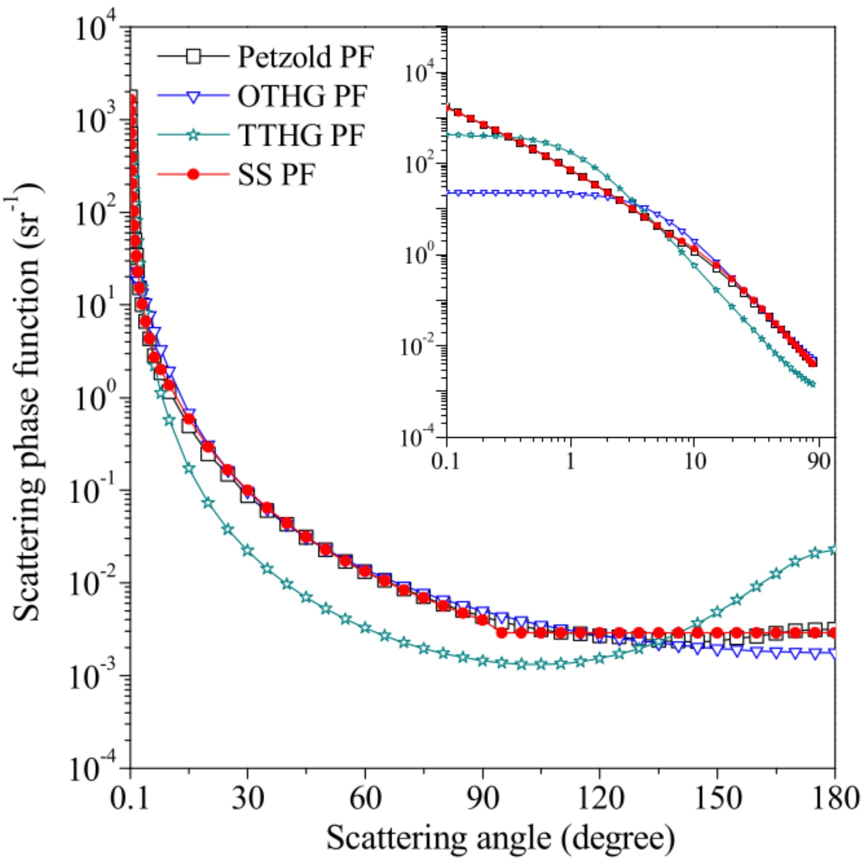

FIGURE 3.8: Comparison of the particulate phase functions with the Petzold's average particle phase function (reference) in a semi-log plot. [34]

3.4.3 Radiative Transfer Equation

The radiative transfer equation is based on the conservation of energy of an underwater beam of light. It takes into account losses and gains of the initial beam, it's formalism is base on the the definitions of water properties described above and the radiance of the beam. The radiance L is given by [31]:

$$L(z, \lambda, \phi, \theta) = \frac{P(z, \lambda, \phi, \theta)}{\Delta A \Delta \Omega \Delta \lambda} \tag{3.15}$$

where ΔA is the area of the detector, $\Delta\Omega$ is the solid angle in the direction of ψ, θ , and z is the distance along the beam propagation direction. The radiance has units $Wm^{-2}sr^{-1}nm^{-1}$. The radiative transfer equation for an homogeneous medium, with only elastic scattering, and without internal sources like possible bioluminescence, is

$$\cos(\theta)\frac{dL(z;\lambda;\theta;\phi)}{dz} = -c(z,\lambda)L(z;\lambda;\theta;\phi) + \int_{4\pi}\beta(z;\lambda;\theta' \rightarrow \theta;\phi' \rightarrow \phi)L(z;\lambda;\theta';\phi')d\Omega' \tag{3.16}$$

here $L(z, \lambda, \phi, \theta)$ is the radiance at propagation distance z in direction θ, φ. The first term on the right, $-c(z, \lambda)L(z; \lambda; \theta; \phi)$ is simply the Beer's Law loss, and the second term is the gain from light scattering from angle θ', ϕ' into direction θ, ϕ.

As said in the previous chapter, this equation is very difficult to solve. In this thesis we present and use a Monte Carlo simulation tool that solves this equation numerically with statistical methods and physical methods for an optical transmitter and a multi lens receiver scheme.

Chapter 4

Monte Carlo Photon Propagation Algorithm

In this chapter, a Monte Carlo numerical method to solve the Radiative Transfer Equation for photon propagation underwater will be described. The basis of the propagation algorithm is very well described in literature principally the work of Cox in his PhD thesis [35]. So only the necessary to understand the algorithm will be presented and emphasis will be given to the features added to the algorithm, which are the main point of this master thesis.

4.1 Assumptions and Approximations

In order to be possible to simulate the underwater channel some assumptions and approximations had to be made:

- Homogeneous medium - scattering and absorption effects don't have a spacial dependency
- Elastic scattering - collisions between photon and water particles are considered to be elastic and therefore no shifts in wavelength occur, in other words, no Raman scattering occurs.
- Simulation boundaries are perfectly absorbing. No photon propagates backwards after passing the sensor plane.

4.2 The Algorithm

The code is divided in two parts, first photon emission and propagation and second photons sensing. The photons propagation flowchart is shown on.

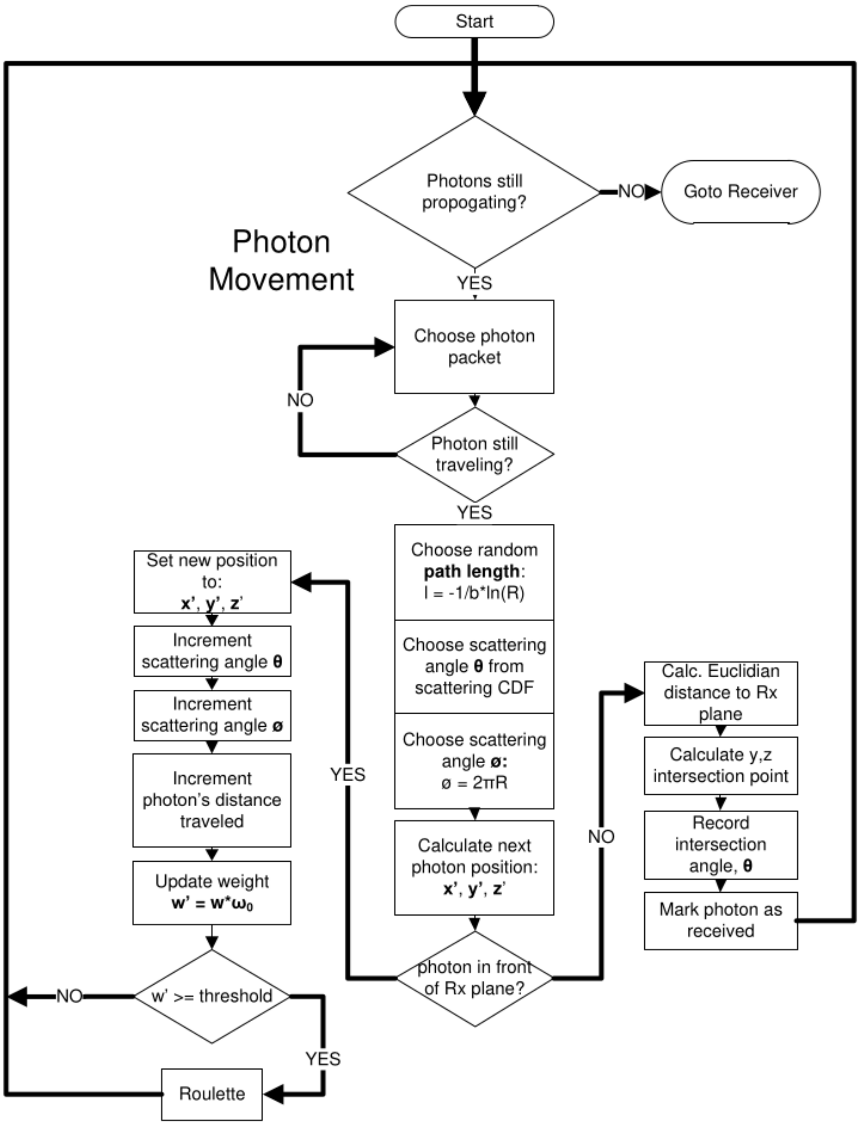

FIGURE 4.1: Flowchart of the Photon Propagation Algorithm [35]

4.2.1 Coordinate System

The algorithm geometry uses a Cartesian coordinate system where the receiver plane is situated on a fixed point in the x/y-plane. The emitter is pointed in the z direction, which will also be referred as the optical axis along this work.

4.2.1.1 Emitter and Photon Initial Conditions

To start propagating photons through the medium, they must start with a given position and vector of propagation that properly simulates a laser beam. Photons start in the plane $z = 0$ and their initial positions, (x_0, y_0, z_0), in Cartesian coordinates, are given from a sampled Gaussian distribution with a given standard deviation equal to the laser beam waist radius w0:

$$\rho(r)=\exp(\frac{-r^2}{2\mathrm{w}_0}) \tag{4.1}$$

Given a sampled radius, the x,y positions are easily calculated:

$$x_0 = r\cos(\phi) \tag{4.2}$$

$$y_0 = r\sin(\phi) \tag{4.3}$$

After having the initial position, to calculate the initial direction for each photon, we need to simulate the emitter's divergence. An hypothetical lens located at the emitter side next to the laser provides the mathematical basis for defining the beam divergence. The focal distance f_l, of this lens will depend on the desired half-angle beam divergence ψ_{div}, and on the laser beam waist radius, and is given by [35]:

$$f_l = \frac{\mathrm{w}_0}{\psi_{\mathrm{div}}} \tag{4.4}$$

The initial polar angle of each photon is then calculated by the ray transfer matrix analysis using the paraxial approximation. We define the optical ray coordinates (h, β), where h is the height and β the slope angle relative to the optical axis. The effect of the lens on the initial ray coordinates is obtained by a multiplication with the optical element matrix of the lens, given by [36]:

$$\begin{bmatrix} h_1 \\ \beta_1 \end{bmatrix} = \begin{bmatrix} 1 & 0 \\ -1/f_l & 1 \end{bmatrix} \begin{bmatrix} h_0 \\ \beta_0 \end{bmatrix}. \tag{4.5}$$

For each photon, the initial azimuthal angle ϕ_0 is taken randomly from $[0, 2\pi]$ since the beam is radially symmetric. This is done by trowing a random number q uniformly distributed between $[0, 1]$ and multiplying by 2π:

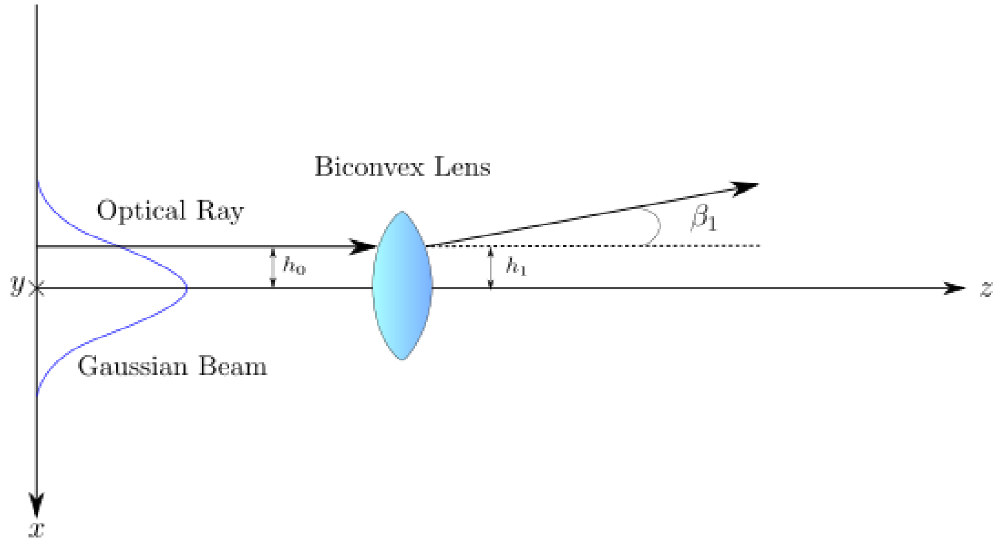

FIGURE 4.2: Scheme of the opening of the optical beam passing it through a lens.

$$\phi = 2\pi q \tag{4.6}$$

Given a certain point P in space with origin O, the azimuthal angle is defined as the angle between the positive x-axis and the projection of the line segment OP on the xy plane.

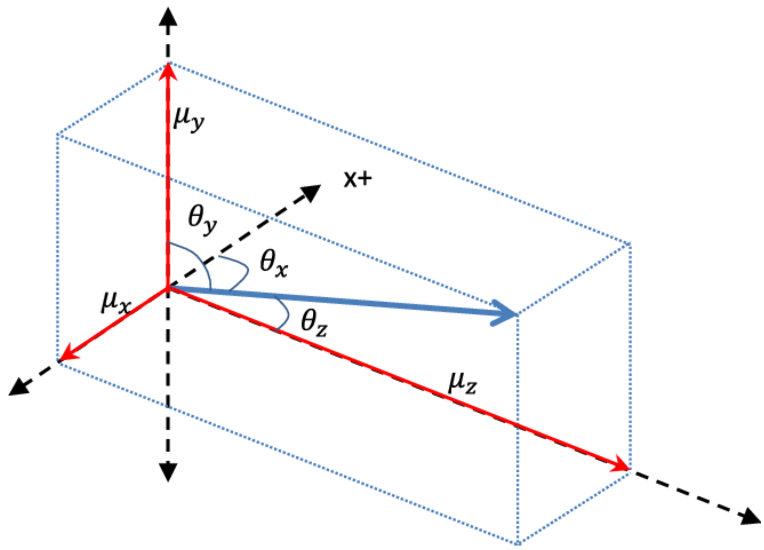

FIGURE 4.3: Illustration of direction cosines. The blue vector represents the photon's direction vector,the red vectors, (μ_x, μ_y, μ_z), are the projections of the photon's direction vector onto the x,y and z axis. axes.

To avoid complex and computation time consuming trigonometric functions, the photon direction vector is divided into his projections on the 3 axis. These projections are called the direction cosines, are illustrated on 4.3, and are defined by:

$$\mu_x = \cos(\theta_x) \tag{4.7}$$

$$\mu_y = \cos(\theta_y) \tag{4.8}$$

$$\mu_z = \cos(\theta_z) \tag{4.9}$$

Here, $(\theta_x, \theta_y, \theta_z)$ are the angles between the propagation vector and the Cartesian axis, respectively. They must comply with the normalization:

$$\mu_x^2 + \mu_y^2 + \mu_z^2 = 1 \tag{4.10}$$

4.2.2 Photon Propagation

The photon path length is the distance at which the photons travels in a homogeneous medium between interaction, which can be absorption or scattering, or both as we'll see next.

The probability of travel over an optical scattering path-length of l is given by [31]:

$$P_l(l) = 1 - e^{-l} \tag{4.11}$$

A typical method to obtain a sample from a given probability distribution function is the Inverse Transform Sampling [37]. Since 4.11 is a invertible function, to obtain a sample we simply need to invert it:

$$l = -\log(1 - P_l(l)) \tag{4.12}$$

and throw a random uniformly distributed number between $[0, 2\pi]$, this number is represented by $P_l(l)$.

Given that the optical path-length is defined as:

$$l = cr \tag{4.13}$$

where c is the attenuation coefficient and r is the geometric distance between optical events, it then comes naturally that r is given by:

$$r = -\frac{1}{c}\log(P_l(l)) \tag{4.14}$$

4.2.3 Absorption - Photon Weight and types of Monte Carlo Algorithm

There are several Monte Carlo Methods to solve the RTE and their difference lies on what happens to the photon at each event, absorption, scattering, both, and how to quantify absorption. All methods are equivalent according to [30]. The two main methods are:

- *Albedo-weight method* (AW) Photons are seen as light packets which start the computation with a given initial weight $w_0 = 1$. At each event, the photon weight will be diminished multiplying it by the albedo coefficient and the photon will also be scattered:

$$w_{n+1} = w_n \omega_0 \tag{4.15}$$

- *Albedo-rejection method* (AR)

  Photons are seen as individual particles which "die" if they are absorbed. An event is either an absorption or a scattering and this is randomly decided by trowing a random uniformly distributed number q between $[0, 1]$ and comparing with the albedo coefficient. Since the albedo coefficient is defined in 3.8 as the ratio between the scattering coefficient and the absorption coefficient, the decision of which event based on:

$$event = \begin{cases} \text{scattering,} & \text{if } q \leq \omega_0 \\ \text{absorption,} & \text{otherwise} \end{cases} \tag{4.16}$$

It is computationally wasteful to terminate a photon before it reaches the receiver plane, so in this thesis the Weight Method was chosen.

4.2.4 Scattering

Each successive scattering event causes the trajectory to rotate its local coordinate frame by θ, φ. Given a volume scattering function $\widetilde{\beta}(\theta)$, the new angle θ' is given by solving the following equation:

$$q = \int_0^{\theta'} \widetilde{\beta}(\theta)\sin(\theta)d\theta \tag{4.17}$$

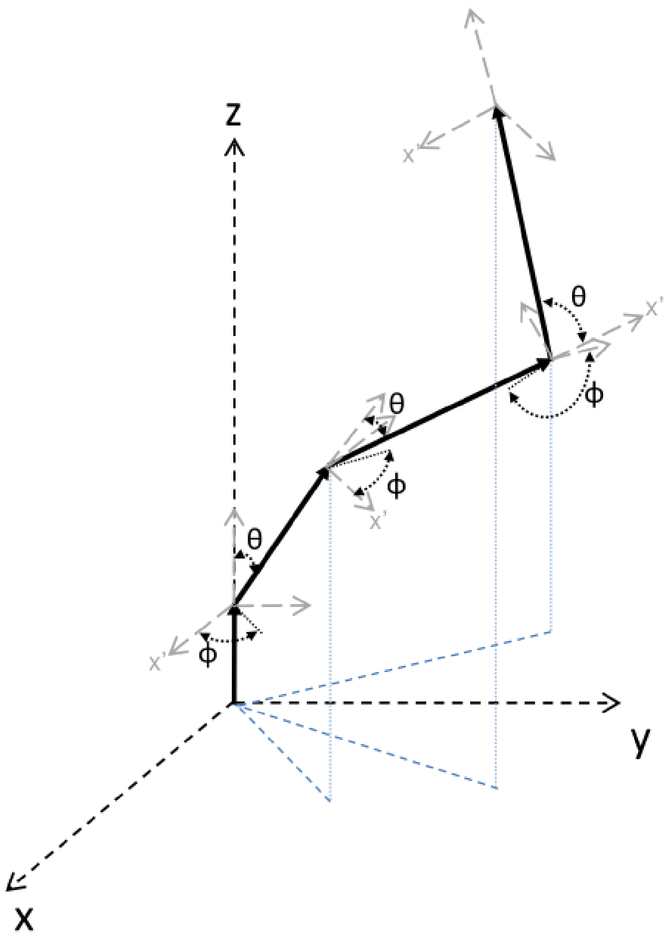

FIGURE 4.4: Photon propagation illustrated. Each scattering event changes the photon's trajectory and therefore it's θ, ϕ, [35].

Where q is another random uniformly distributed number between $[0, 1]$.

The new azimuthal angle ϕ' is independent of any probability density function, and therefore is sampled uniformly between $[0, 2\pi]$.

4.3 Validation of Simulation Model

The photon propagation algorithm validity was confirmed by comparing with experimental results of on-axis laser beam propagation through a closed 3.6 m water tank, taken by Cox in [38]. The communication system was composed of an emitter, a 532nm diode-pumped solid-state laser of 2 mm beam diameter and divergence ¡1.5mrad and a receiver, a 25.4mm achromatic biconvex lens at 75mm focal distance of a PMT (photomultiplier tube) unit with an 8 mm active area. The laser was considered collimated in the simulation. The different levels of water attenuation coefficients were obtained by adding

Maalox as a scattering agent. This is the same scenario in which Cox's code was validated. The average power was measured as a function of the attenuation coefficient. The same scenario was simulated. The normalized intensity power was plotted versus the attenuation coefficient in 4.5. Good agreement is seen for all the points in which the simulation was made.

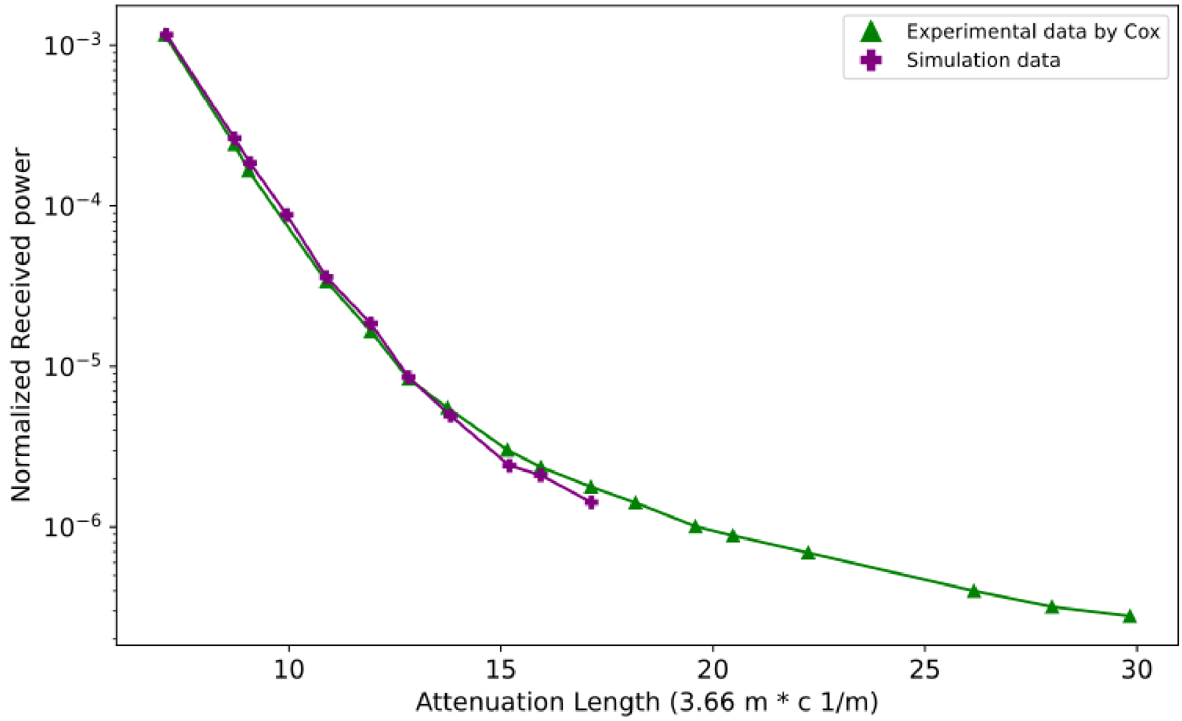

FIGURE 4.5: Validation of results - Comparison with Cox's experimental data of a 3.6m water tank with different attenuation coefficients made by adding different quantities of scattering agent Malox.

4.4 Emitter and Sensor Rotation

In the traditional code implementation of the "Photonator" by Cox on [35], the emitter is pointed along the z-axis. In this work, we added the ability to rotate the emitter along any direction given a direction vector ω, as represented in 4.6. An efficient routine that constructs a 3-dimensional rotational matrix that rotates any unit vector $\mathbf{f}$ into ω by an angle α was used [39].

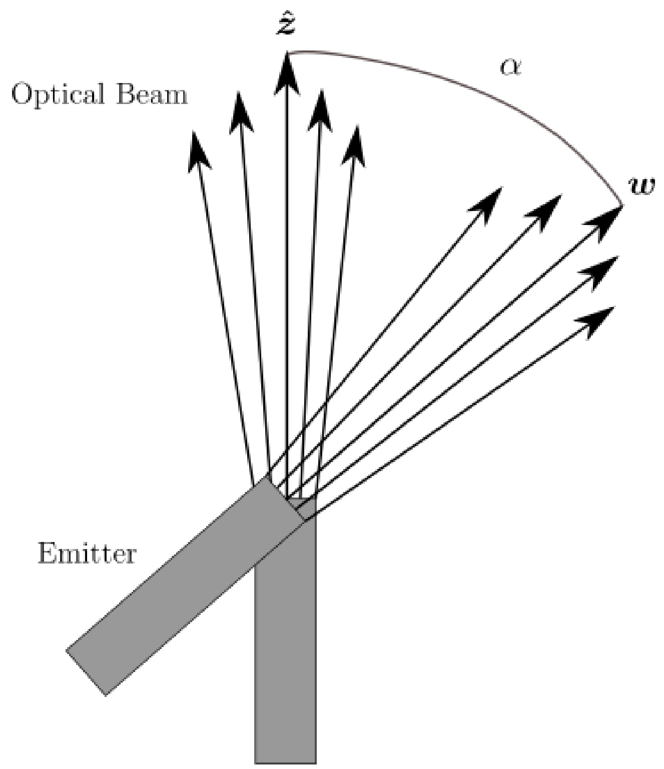

FIGURE 4.6: Rotation of the emitter direction. From the default $\hat{\mathbf{z}}$ direction to any desired vector ω

This routine has no square-roots or trigonometric functions, speeding computation time. In this case ω is the unit vector on the z axis that we define as $\hat{\mathbf{z}}$. To help simplifying, we define $\mathbf{s}$, with vector components (s_x, s_y, s_z), as the vector product of $\hat{\mathbf{z}}$ and ω as:

$$\mathbf{s} = \hat{\mathbf{z}} \times \mathbf{w} \tag{4.18}$$

and q as the dot product of $\hat{\mathbf{z}}$ and $\mathbf{w}$, written as

$$q = \hat{\mathbf{z}} \cdot \mathbf{w}. \tag{4.19}$$

From these we define another auxiliary variable m written as

$$m = \frac{1-q}{1-q^2} = \frac{1-q}{\mathbf{s}\cdot\mathbf{s}}. \tag{4.20}$$

This way a simple version of this rotation matrix emerges as

$$R(\mathbf{f}, \mathbf{w}) = \begin{bmatrix} q + ms_x^2 & ms_xs_y - s_z & ms_xs_z + s_y \\ ms_xs_y + s_z & q + ms_y^2 & ms_ys_z - s_x \\ ms_xs_z - s_y & ms_ys_z + s_x & q + ms_z^2 \end{bmatrix}. \tag{4.21}$$

In 4.7 an example of the angularly misaligned communication is presented. The angle of rotation of the emitter and of the plane of sensors are given respectively by γ_e and γ_s.

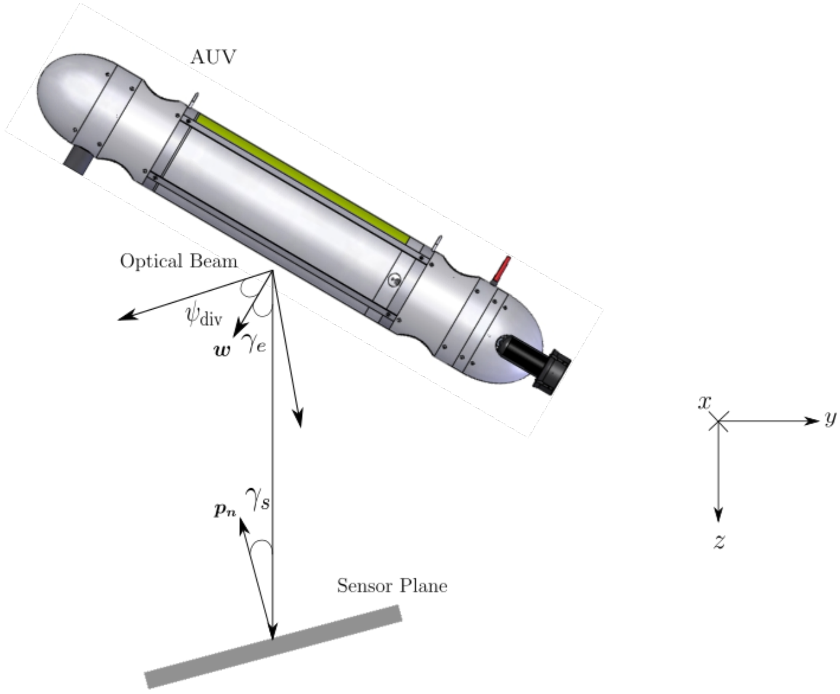

FIGURE 4.7: AUV communicating with fixed receiver. Both emitter and receiver have the same radial direction ϕ but are rotated in relation to the z-axis, by the angles γ_e and γ_s respectively.

The photons are propagated using the Photonator algorithm. To be able to simulate an architecture of sensors in a plane rotated with regard to the emitter, the condition of termination of each photon had to be changed. Instead of finishing the photons in a given finish plane, $z = z_f$, they are finished in a general plane given by its normal vector p_n (p_{nx}, p_{ny}, p_{nz}). After every displacement of the photons, their new position (x', y', z') will be evaluated. If the photon is past the plane, the following statement given as

$$p_{nx}x' + p_{ny}y' + p_{nz}z' > cz_f \tag{4.22}$$

will be true. Then the intersection with the plane is calculated and the photon's data, position in the final plane, the vector of propagation and weight will be saved in a file for posterior analysis.

4.5 Sensor Architecture

Different sensor architectures were analysed in this work. All are composed with a different number of lens sensor pairs, located at different positions inside an external circle.

4.5.1 Accurate Lens Behaviour

Another innovative feature added to the Monte Carlo method is the ability to simulate accurately the refraction of photons when these pass through the lens. Since photons are treated individually in this method, one accurate way is to calculate the refraction on each surface of the lens for each photon. Mathematically the biconvex lens used is treated as two parts of spheres with a thickness in between. After calculating the intersection of the photons with the first interface of the sphere, the vectorial Snell's Law is applied. We define θ_1 as the angle of incidence with the normal of the sphere g_i and $\cos(\theta_1) = -g_i \cdot v_i$, where v_i is the vector of propagation of the photon. The vector of propagation after the first refraction v_{r1} is given by [40]:

$$v_{\mathrm{r1}} = \frac{n_1}{n_2} v_i + \left(\frac{n_1}{n_2} \cos\theta_1 - \cos\theta_2 \right). \tag{4.23}$$

Where the following definitions were used

$$\sin\theta_2 = \frac{n_1}{n_2} \sin\theta_1. \tag{4.24}$$

After the first refraction, on the interface defined as ξ_1 that separates n_1 from n_2, the photon is propagated through the glass until the next lens surface. Here the photon meets another interface between n_2 and n_3, ξ_2, where the same refraction calculation is made with the new vector and refrative indexes.

4.5.2 Packing

The position of the lenses were chosen from known results of proven packing algorithms of circles into circles [41]. After defining an N number of lenses and having their packing positions, another lens in the centre is added with the maximum possible radius. 4.9 depicts a diagram of the positions of the various lenses for a number of lenses from 4 to 7.

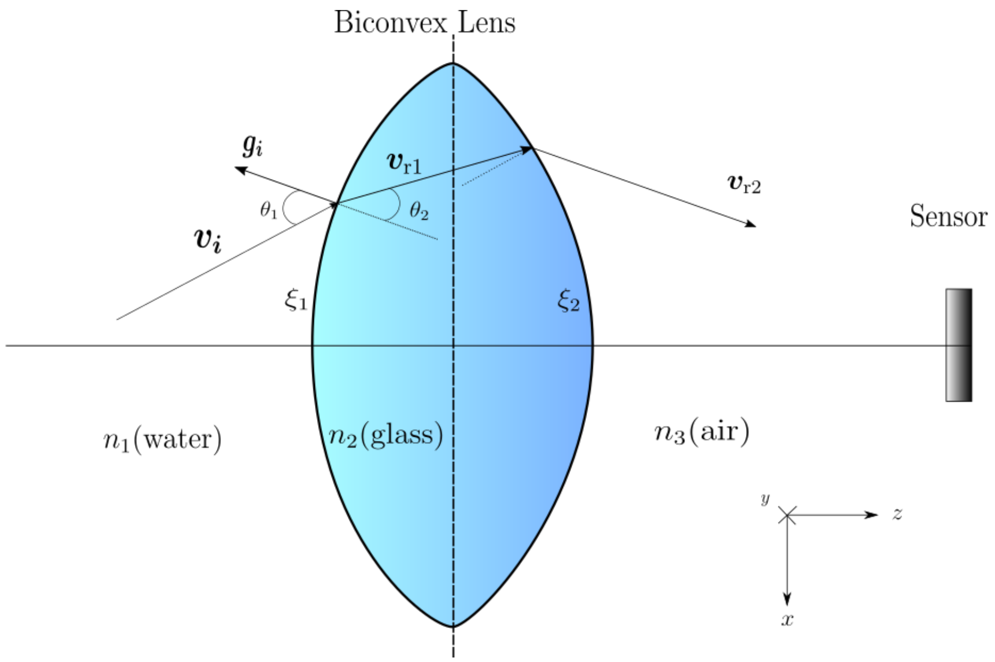

FIGURE 4.8: Photon as ray vector being refracted at both medium interfaces. The lens directs the photons to the sensor.

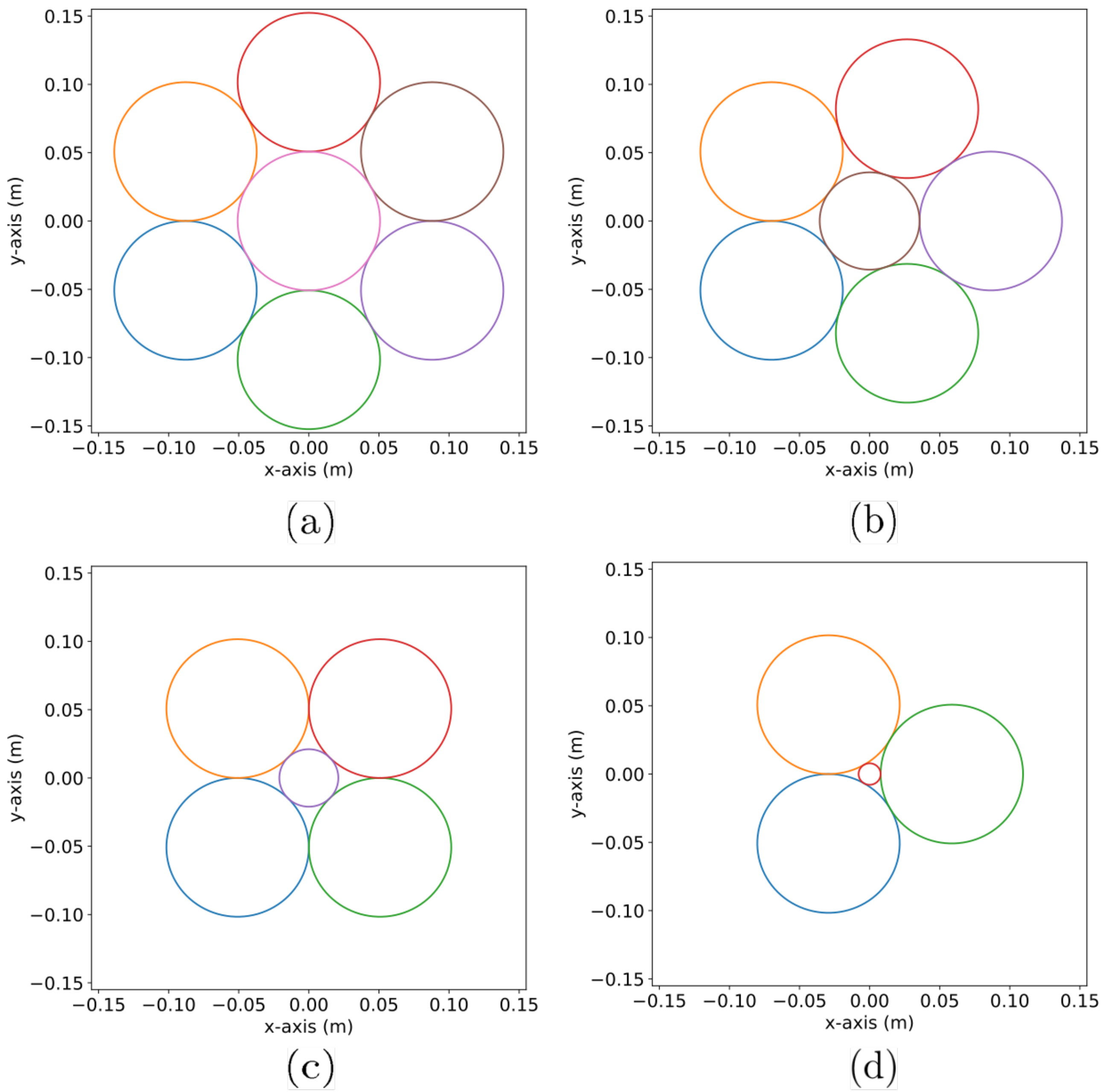

FIGURE 4.9: Scheme of N sensors given by "circles inside circle" packing algorithm. (a) N=7; (b) N=6; (c) N=5; (d) N=4.

Chapter 5

Prediction and Optimization Techniques used

5.1 Particle Swarm Optimization

In computational science, particle swarm optimization (PSO) is a population based computational method that optimizes a problem by iteratively trying to improve a candidate solution with regard to a cost function. We start with a number of particles or agents that have a position and a velocity. The goal is this swarm of particles based on search and intelligence converge to a optimal solution. Position is just a point in the N dimensional search space of variables we want to optimize. The position of each particle is given by [42]:

$$X_i^T = (x_{i1}, x_{i3}, x_{i3} x_{i4}, x_{in})^T \tag{5.1}$$

And the velocity at the next algorithm iteration:

$$V_{ij}^{t+1} = \omega V_{ij}^t + c_1 r_1^t (pbest_{ij} - X_{ij}^t) + c_2 r_2^t (gbest_j - X_{ij}^t) \tag{5.2}$$

Where *pbest* it's the best result that the particle i ever found.

And *gbest* it's the best result that the whole groups of particles (swarm) ever found.

This analysis is made based on a given cost function that you want to minimize.

The parameter ω it's just an inertia factor, higher values result in a higher dependency of the next velocity from the last one.

The parameter c_1 it's an individual intelligence factor.

The parameter c_2 it's an social intelligence factor

The velocity is more like a displacement that a velocity but it's the term used. At each iteration the next position is given by:

$$X_{ij}^{t+1} = X_{ij}^{t} + V_{ij}^{t+1} \tag{5.3}$$

The searching algorithm stops when it reaches a limit number of interaction or when the difference of when the difference in cost function of two consecutive points is lower than a given threshold.

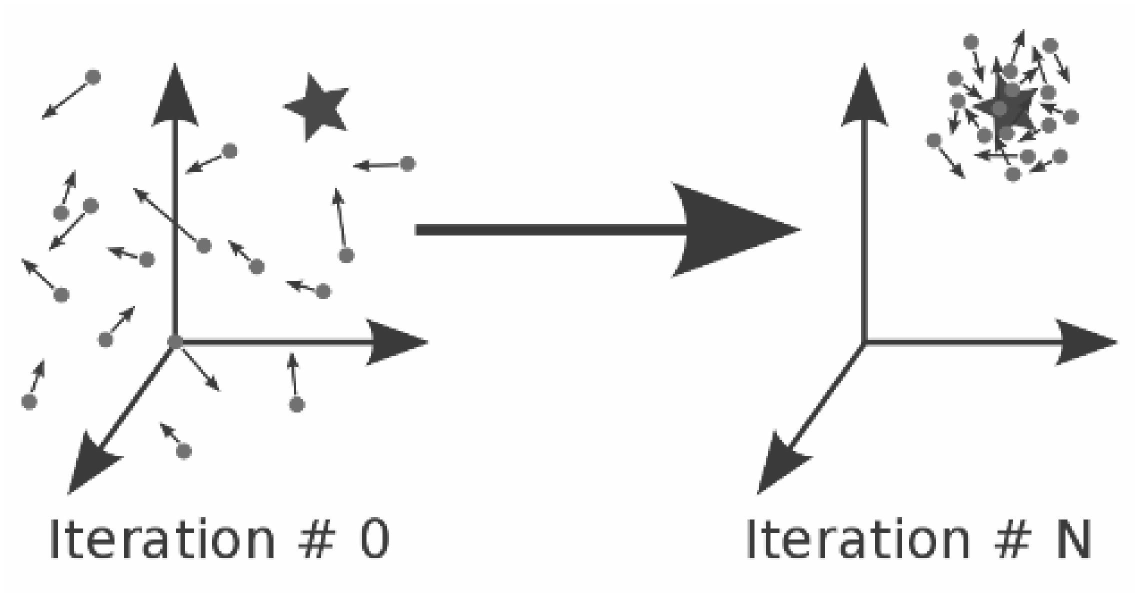

FIGURE 5.1: Particle Swarm Optimization

5.2 Decision Tree and Random Forest Learning

5.2.1 Decision Tree

A decision tree is a decision support tool which uses a tree-like model of decisions and their possible consequences. It is one way to display an algorithm that only contains conditional control statements. In a decision tree each internal node denotes a test on an attribute, each branch represents an outcome of the test, and each leaf node (terminal node) holds a class label [43]. The goal is to create a model that predicts the numerical value of a target variable based on the input variables. There are several stochastic algorithms that find a decision tree for a given data set of features and labels but the explanation of these algorithms is beyond the scope of this thesis. We used built algorithms as a black box.

On figure 5.2 an example of a typical regression tree for Prediction of the Medium Home Value is shown.

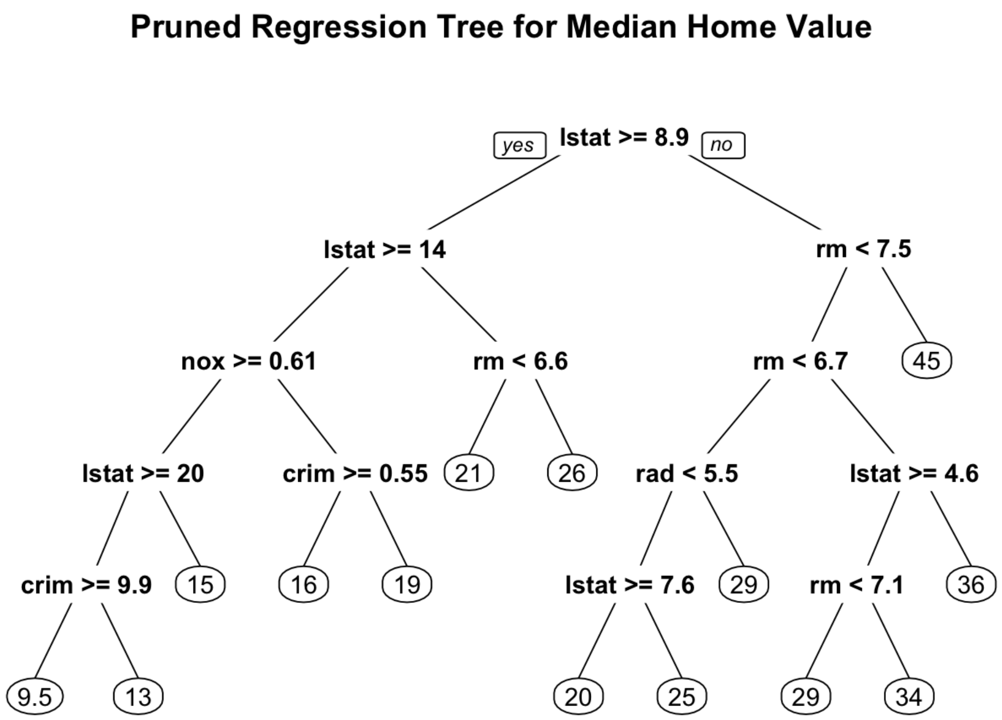

FIGURE 5.2: Regression Tree for Medium Home Value

5.2.2 Random Forest

Random Forest is Supervised Learning algorithm which uses an ensemble learning method, that is it combines predictions from multiple machine learning algorithms, in this case from multiple Decision Trees. In a random forest algorithm the trees in are run in parallel, which means that there is no interaction between them [44].

Random Forest are one of the most accurate learning algorithms, as seen on 5.3, their output is the average of the output of several decisions trees.

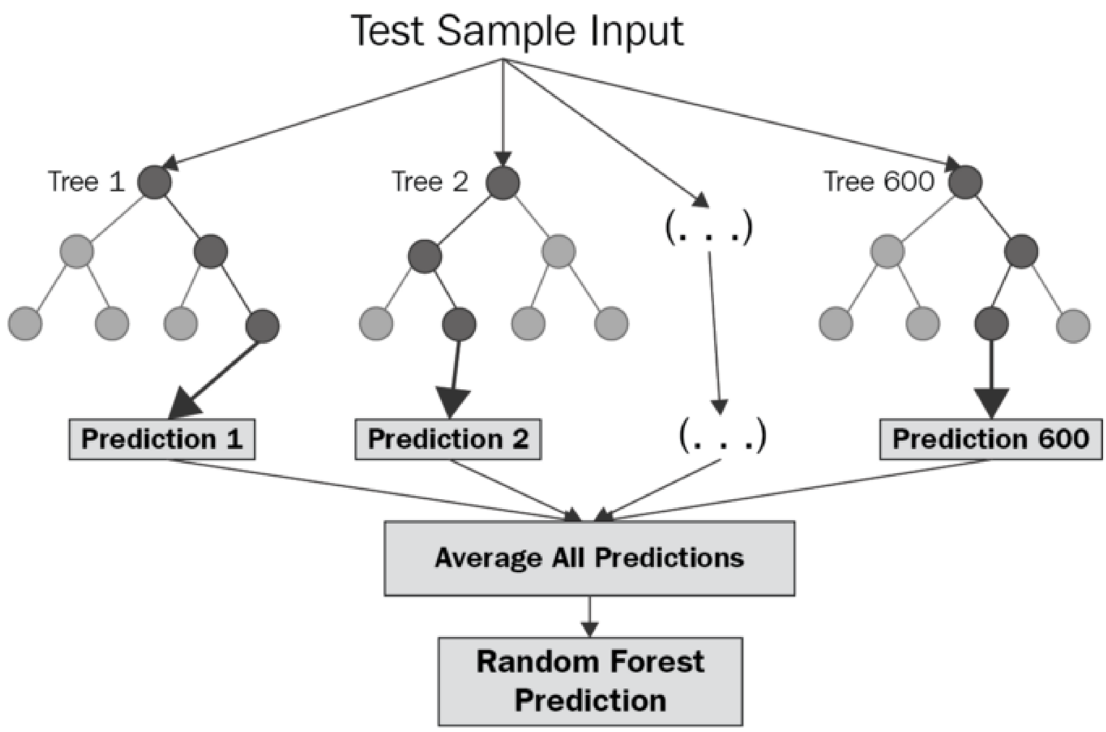

FIGURE 5.3: Random Forest Structure

Chapter 6

Results

6.1 General Simulation Parameters

TABLE 6.1: Simulation Parameters

Parameters	Value
Number of Photons	1×10^6
Wavelength λ	520 nm
Refractive index of water	1.33
Refractive index of lens	1.44
Tx (emitter) beam waist radius	1 mm
Tx (emitter) divergence	[0-60]°
Rx (sensor) radius	10 mm
Lens thickness	15.6 mm
Lens curvature radius	52.6 m
Lens diameter	101.6 mm
Lens focal distance	60 mm
Number of Lenses (N)	[4-7]
Distance between Tx and Rx	[0.5-1] m
Misalignment angle between Tx and Rx	[0-10]°

6.2 Equivalence of Monte Carlo Methods

In order to confirm the results of the equivalence of the different Monte Carlo methods from [30] the same validation of the algorithm as explained in 4 was made for the Albedo Weigh Method (the one used on this thesis) and the Rejection Method. A graph comparing the experimental results and both methods can be seen on 6.1

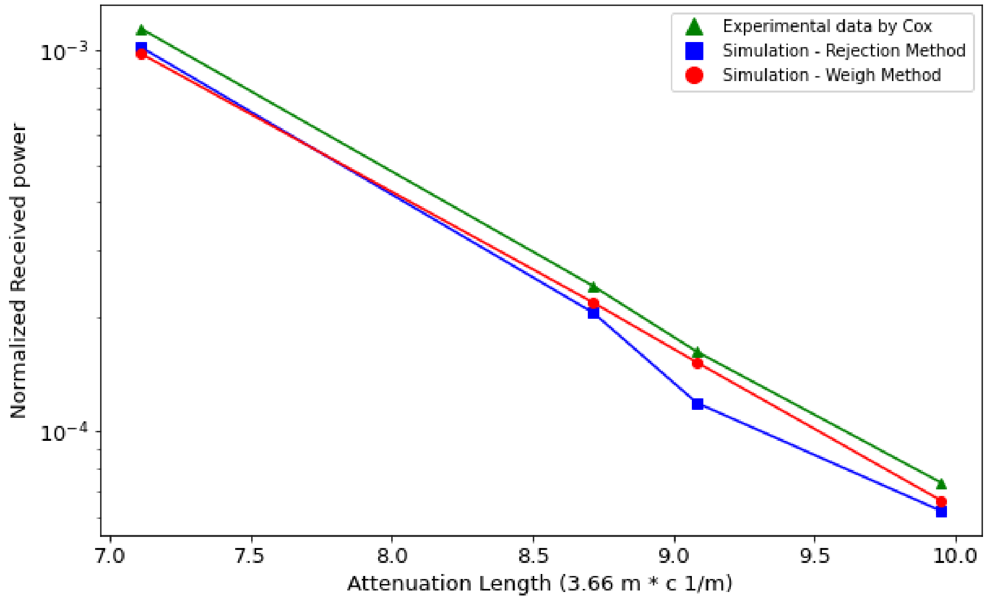

FIGURE 6.1: Comparison of the Monte Carlo methods

6.3 Link Misalignment analysis

Evaluation Algorithm

For each scenario composed of water type, total distance, the divergence and vector of propagation of the emitter and plane of the final sensor, the photons are propagated using the modified Photonator, their final parameters, as mentioned on section 2B, are stored in a data file. An evaluation algorithm was created to analyse this data in terms of received power and MALO for each architecture. For each data file corresponding to a given scenario, the receiver architecture is simulated, and the received power is calculated. The algorithm is sufficiently general to consider the case where the misalignment is due to both the transmitter and receiver being misaligned at a certain angle and simultaneously being offset between each other. In the latter case the offset does not have circular symmetry, in general. Instead of *maximum allowed lateral offset* (MALO), a calculation of the *maximum allowed radial offset* (MARO) was made. This calculation is made by sweeping the lens's and sensor scheme central position on the xy-plane, both angularly and radially, instead of only laterally like MALO. In each of these positions of the lenses scheme, we calculate the received power that would arrive in the sensors. Even if the receiver plane is tilted due to angular misalignment, the lens positions are displaced on the xy-plane

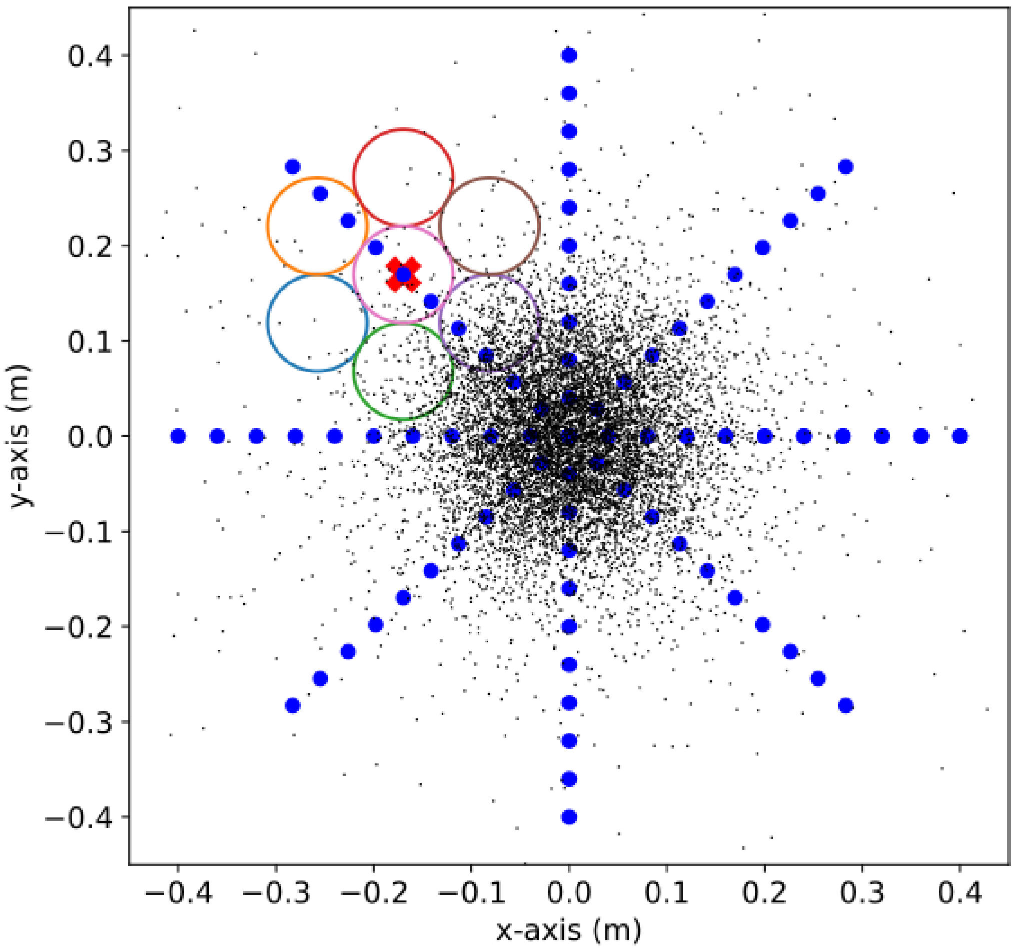

FIGURE 6.2: Moving scheme of sensors for MARO calculation. The sensor scheme is offset through the 2D plane radially from 0 m to 0.4 m and in angle from 0 to 360 degrees in steps of 45 degrees.

which makes this analysis important. After this, another simple routine calculates the maximum radius that the AUV can move for the receiver to have a minimal amount of relative received power. The minimum accepted ratio of received power relative to the transmitted power was of 1×10^{-3}, which is equivalent to considering an emitter with a typical power of 0 dBm and a minimum received optical power of −30 dBm (suitable to achieve the forward error correction limit BER of 3.8×10^{-3} for a data rate of 100 Mbit/s) [45]. In 6.2, we see a the scheme with 7 lenses, where the dark dots mark the various positions the set of lenses are displaced for calculation of the MARO parameter and all the positions (dark dots) the scheme is centred for calculating the received power.

6.3.1 Offset Misalignment Results

6.3.1.1 Types of Water

The first analysis consisted in the calculation of the MARO parameter for different types of water using the fixed parameters from Table. 1, distance between emitter and receiver of 1 metre and a N=7 lenses scheme, the results are shown in 6.3. A characteristic curve is found in all of them. This curve shows an optimal divergence that maximizes the tolerance to the position misalignment of the system. Albeit this work being a more complete analysis of the sensor-lens pair, these results confirm the conclusions of previous published work [1]. An evident difference between different water types is that the MARO is non zero at zero beam divergence for more turbid waters and increases with the water turbidity. This result was expected due to increased scattering that acts as a diverging factor, maximizing the MARO.

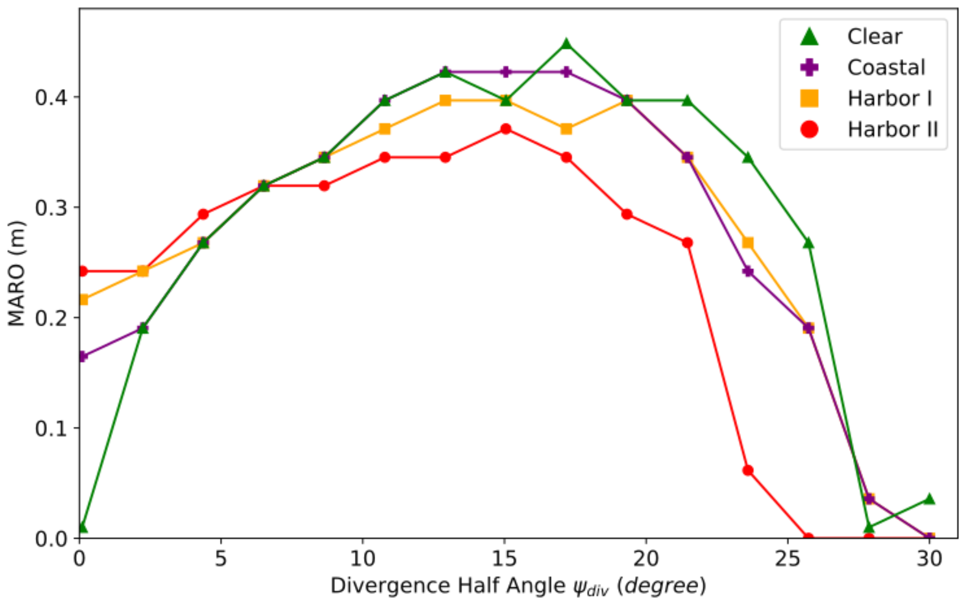

FIGURE 6.3: MARO calculation as a function of the emitter's divergence for different water types. Tx-Rx distance of 1 metre, 7 lenses scheme.

6.3.1.2 Propagation Distance

The same MARO calculation was performed while sweeping the divergence using the parameters from Table. 1 and a N=7 lenses scheme, but in this case, for different lengths between emitter and receiver and only for the two extremes of water turbidity, Clear and Harbor II waters, with the results being plotted in 6.4. The same type of curve that shows a global maximum for a certain divergence is obtained. For a distance of 1 metre, better tolerance than 0.5 m is observed. The higher number of scattering events and the opening of the beam due to propagation might cause this behaviour. On the other hand, above the ideal divergence, the MARO degrades significantly for 1 m. Here, the increased scattering and more significant propagation distance make the beam spread so much that the minimum amount of power doesn't reach the sensors. We observe this same behaviour both for clear waters and Harbor II water, 6.4, showing that the geometry of the link is the dominant factor in such short-range links.

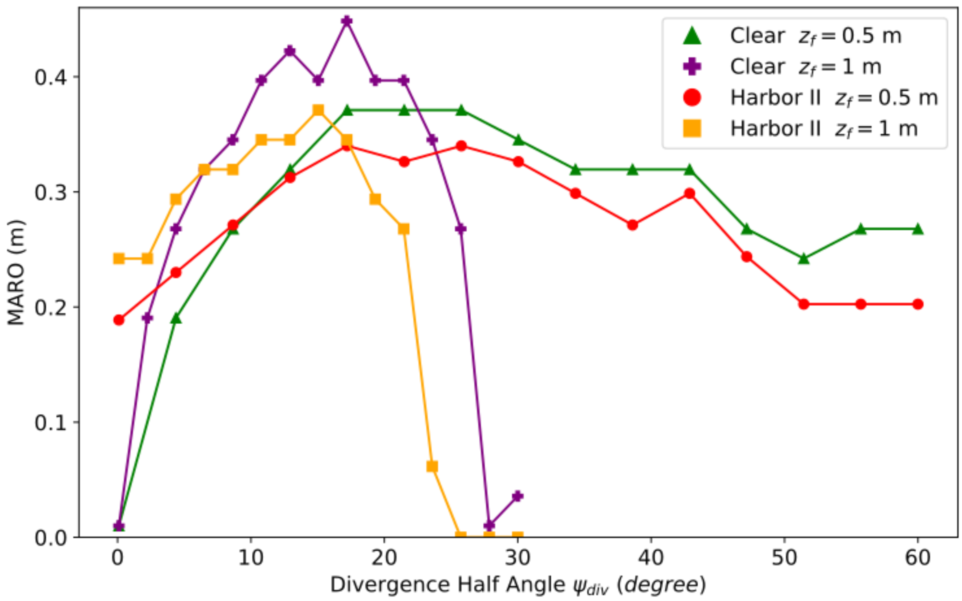

FIGURE 6.4: MARO calculation for different water types at different Tx-Rx distances, N=7 lenses scheme.

6.3.1.3 Sensor Scheme

An analysis of the sensor architecture with sensor positions given by a circles inside circle packing algorithm was simulated to evaluate ways to increase the tolerance to the position and angular misalignment problem. An analysis of the number of sensors of this scheme was made for clear waters and propagation distance of 1 metre on clear waters with the results shown in 6.5. A distinct improvement of the tolerance to misalignment is observed for a higher number of sensors. This improvement is a direct consequence of the higher total receiver area. Having 7 sensors in a packing disposition as depicted in 6.2 increases the MARO by approximately a factor of 3. A gradual increase in the optimal divergence can be seen. This is also expected due to the larger area of the receiver.

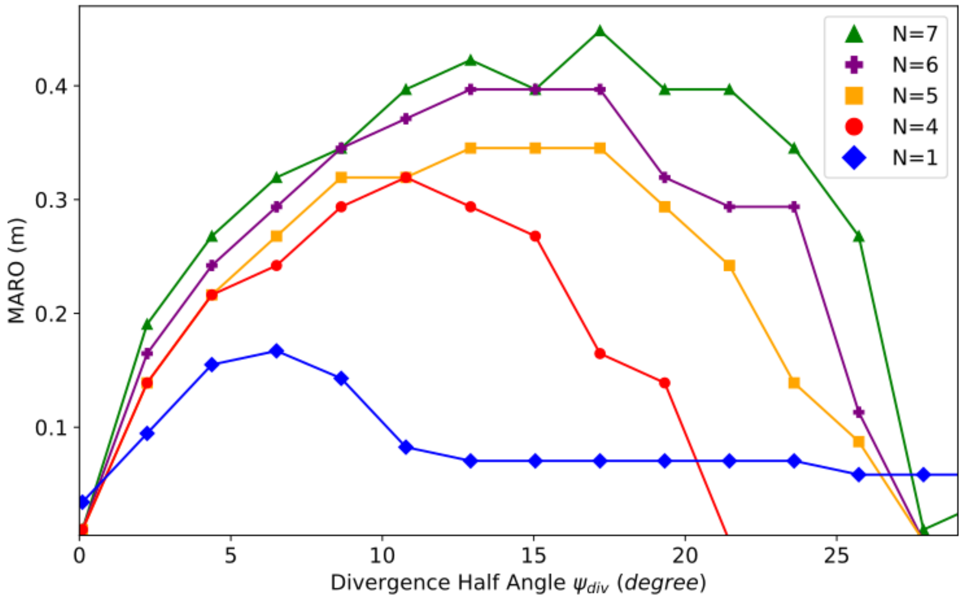

FIGURE 6.5: MARO calculation as a function of the emitter's divergence for different number of sensors on the sensor scheme. Clear waters and Tx-Rx distance of 1 m.

6.3.1.4 Rotation Misalignment

An analysis of the angular alignment of the emitter-receiver system in highly turbid Harbor II waters using a propagation distance of 0.5 metres was made using a 7 lenses scheme. Three different configurations were simulated, (1) aligned system, (2) only emitter rotated into a given direction and (3) only emitter rotated in the same direction.. These analyses were made for angles of 5,10,15, and 20 degrees, in 6.6 the 10 degrees rotation is shown. As expected, we observe a worse performance when either the emitter or the plane of sensors is rotated as shown in 6.7 (a). When the emitter is rotated to compensate for fewer photons arriving at the sensors, an increase in the optimal divergence is seen. The opposite behaviour is observed when the plane of sensors is rotated. The optimal divergence in both kinds of rotations as a function of the angular misalignment is plotted in 6.7 (b).

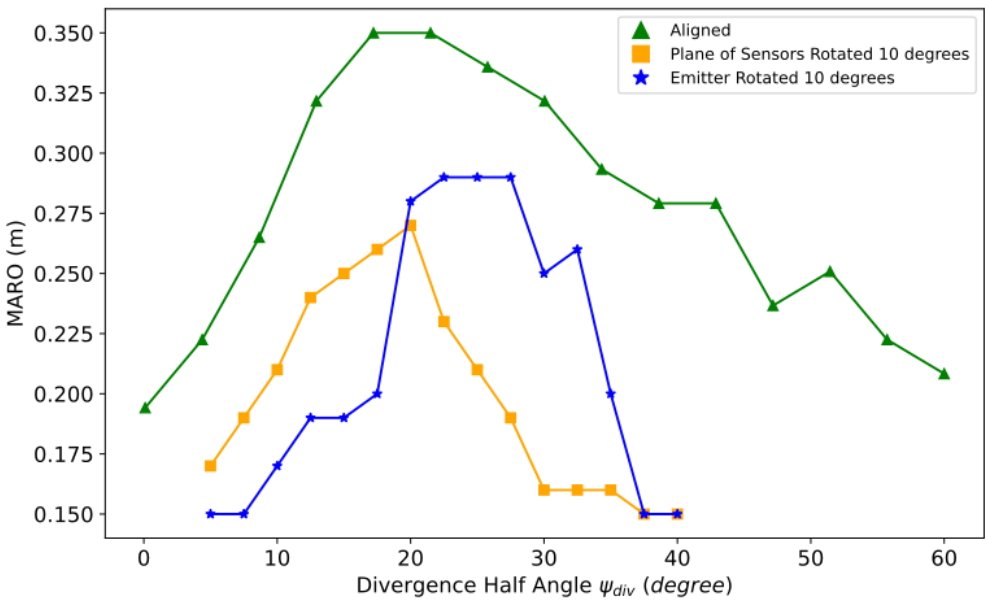

FIGURE 6.6: MARO calculation as a function of the emitter's divergence for rotated communication links. Harbor II waters and Tx-Rx distance of 0.5 metres, N=7 lenses scheme.

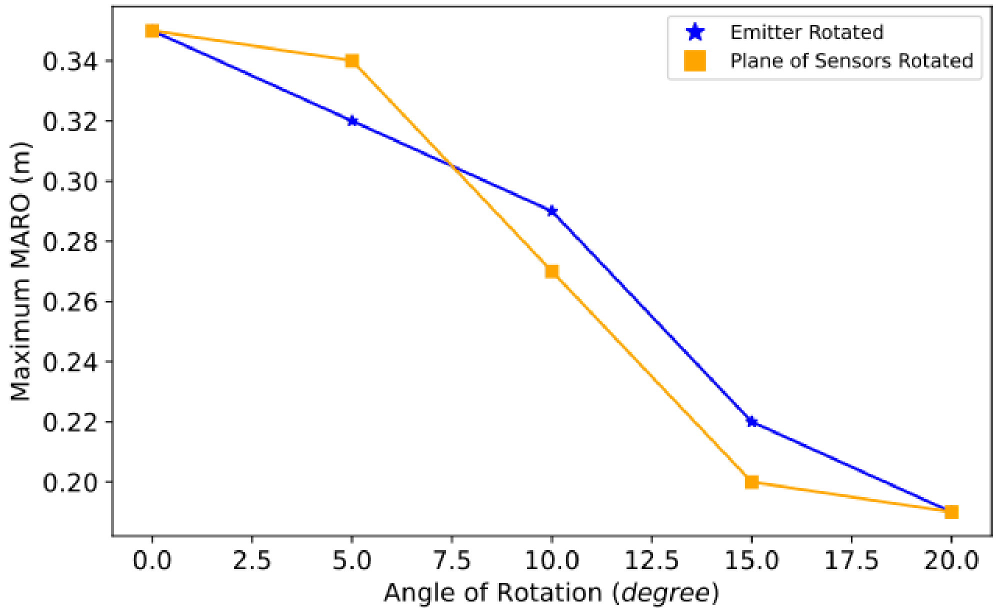

(a)

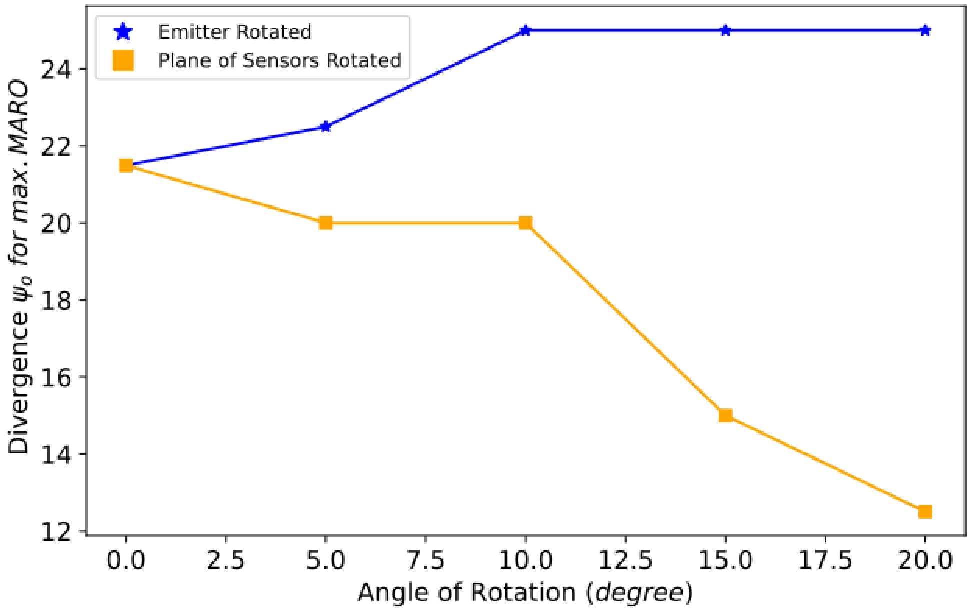

(b)

FIGURE 6.7: Maximum MARO (a) and Divergence for max. MARO (b) and as function of the rotation angle. Harbor II waters and Tx-Rx distance of 0.5 metres, N=7 lenses scheme.

6.4 Lens Scheme Optimization

As shown in 4.9, we tested the link performance with several lenses schemes each with different number of lenses and which positions of each lens were taken from known results of a packing algorithm of ”circles inside circles” [41].

To make sure this was the optimal scheme to maximize the tolerance to misalignment, we added the possibility of a bigger external radius like on figure 6.8

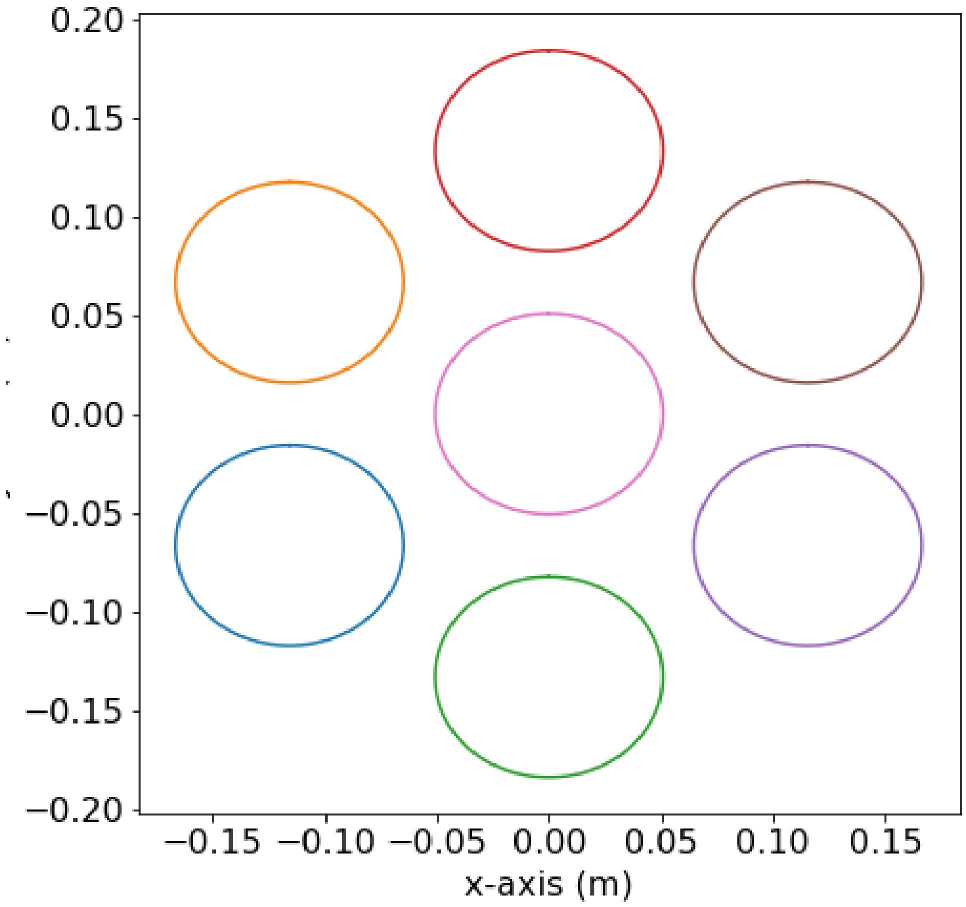

FIGURE 6.8: 7 lenses scheme with external variable external radius

Using a Particle Swarm Optimization we concluded that the optimum radius of the external circle was equal to the minimum radius for each scheme of lenses. The goal here was to make a system more tolerant to offset misalignment therefore, the cost function was built to maximize the MARO.

6.5 Live Misalignment Offset Prediction

As seen in 6.3, in a real communication scenario between a AUV and a fixed sensor, as the one in 6.9 there's an optimum emitter's divergence at which the system is most tolerant to offset misalignment. At this optimum divergence the MARO takes a maximum value. In a live communication scenario with ocean currents, in order to maintain stable communication, the AUV needs to adapt the emitter's divergence, by changing the distance of the laser to the diverging lens, based on much is the present average offset.

We propose a Random Forest machine learning method to identify the offset and angle of the AUV in relation to the fixed sensor at each moment, based on the power distribution of each lens. Using a 7 lens scheme, we train a Random Forest algorithm with a 64x7 matrix, which contains the power received for each lens in each point of a 64 point grid in the AUV r, θ plane. Having a trained algorithm with optimized parameters based on an extensive grid search, we test the algorithm on a different matrix, this time the matrix shows the power received for each lens but at another set of points in space.

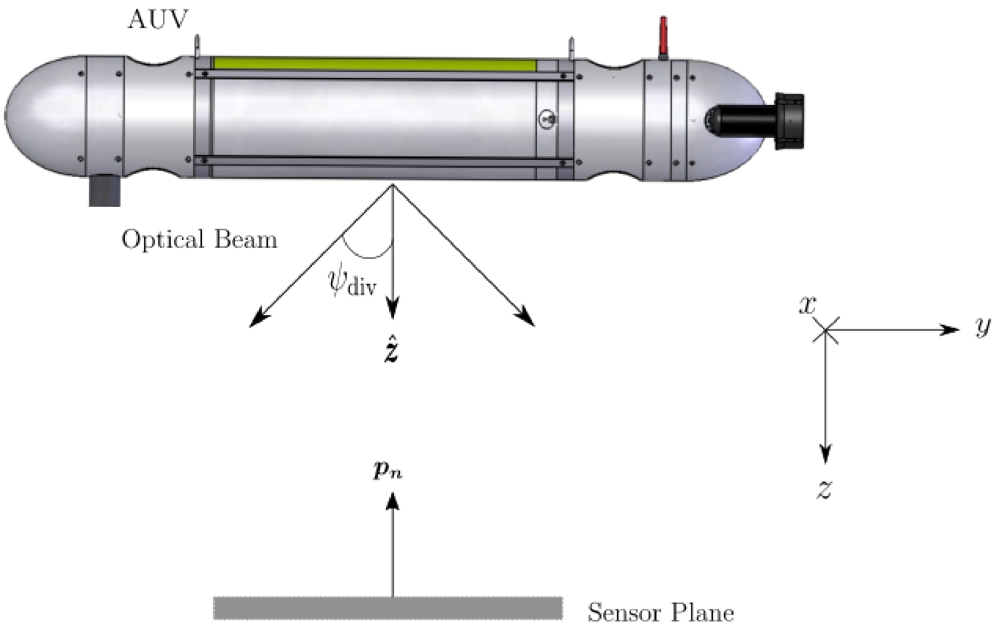

FIGURE 6.9: AUV communicating with fixed receiver using a divergent optical beam.

For a 0.5 meter distance of propagation and Clear water, the half-angle divergence was 10 degrees. The root medium squared error for the predicted radius is 5mm and for the angle is 9degrees. Comparison of predicted results and the actual test data can be see on 6.10 and 6.11.

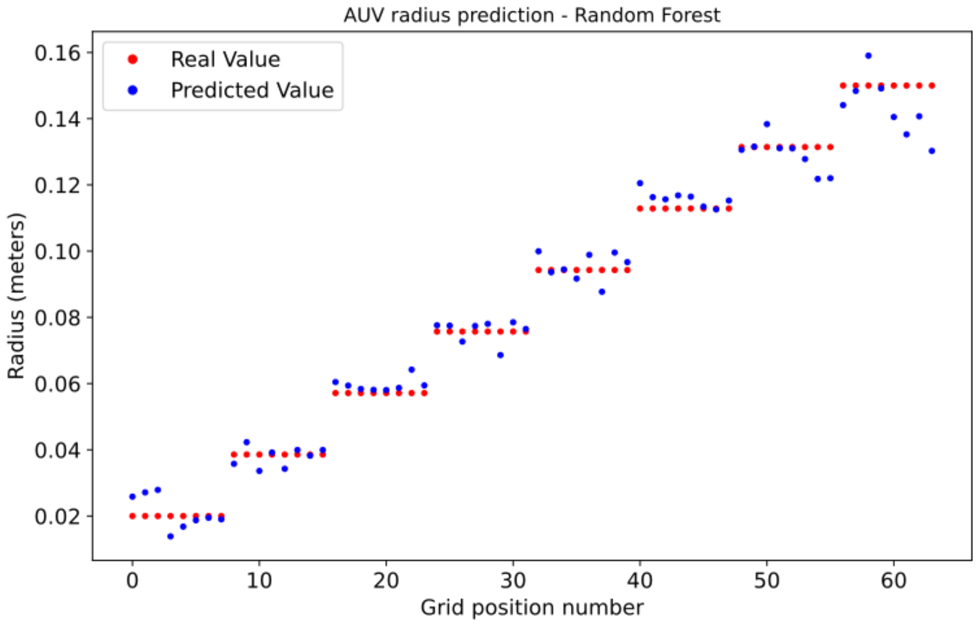

FIGURE 6.10: Visual comparison of the predicted radius and the real value - 0.5m

For a 1m meter distance of propagation and Clear water, the half-angle divergence was 8.5 degrees. The root medium squared error for the predicted radius is 6mm and for the angle is 10degrees. Comparison of predicted results and the actual test data can be see on 6.12 and 6.13.

The optimal Random Forest Parameters found are:

- N estimators: 400
- Minimum samples per split: 2,
- Minimum samples per leaf: 1,
- Maximum features: square root,
- Maximum tree depth: None,
- Bootstrap: False

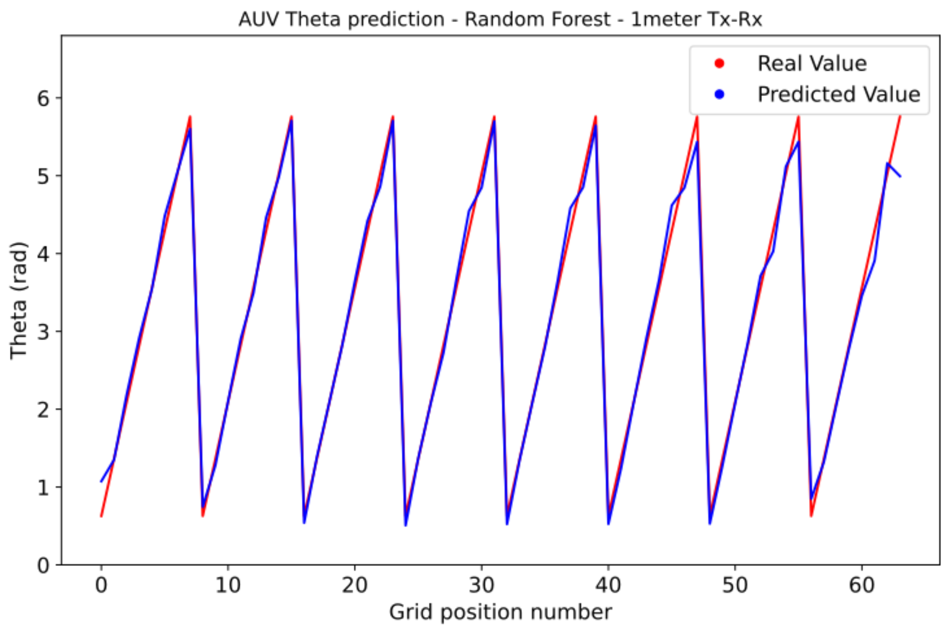

FIGURE 6.11: Visual comparison of the predicted angle θ and the real value - 0.5m

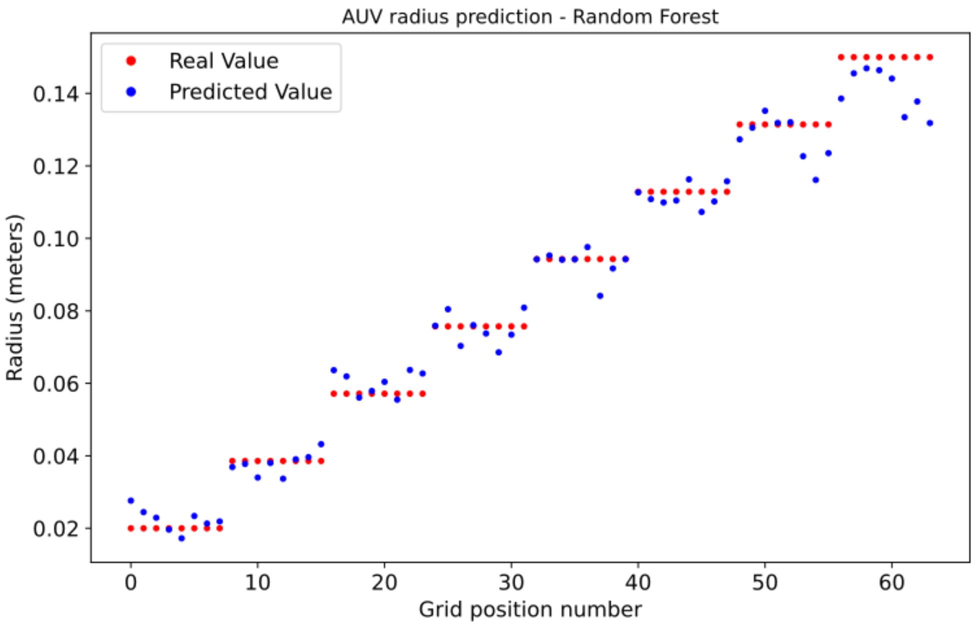

FIGURE 6.12: Visual comparison of the predicted radius and the real value - 1m

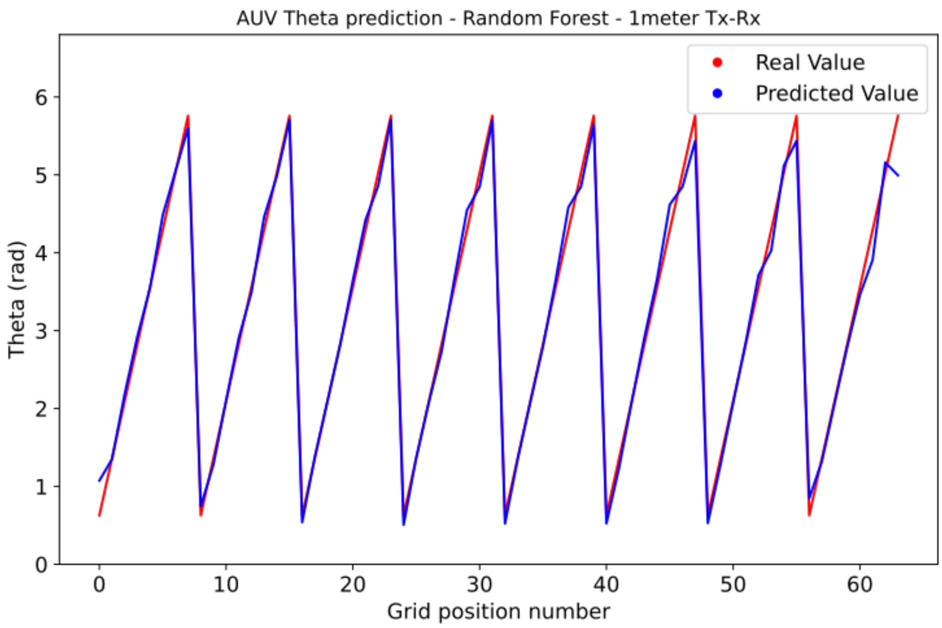

FIGURE 6.13: Visual comparison of the predicted angle θ and the real value - 1m

Chapter 7

Conclusion and Future Work

In this thesis a simulation of photon propagation based on the Monte Carlo method was performed, which models accurately the beam divergence as a way to mitigate misalignment in underwater optical wireless communications. The model includes lateral offset and angular misalignment between the transmitter and receiver in a scheme of several pairs of sensor-lens. A new analysis was presented based on the maximum radial offset that showed the existence of an optimal divergence in agreement with previous results. Novel results for angular misalignment and of different sensor architectures with various lenses, in a scheme circle within a circle, lead to an increased tolerance to misalignment. Some interesting results were achieved. For a 1 metre Tx-Rx distance and seven lenses scheme, the ideal divergence of the emitter's beam is around 15 degrees, independently of the water turbidity. For clear waters and 1 metre Tx-Rx distance and N=7 lenses scheme, the ideal divergence is 17 degrees while for the same configuration, but 0.5 metres of distance, the ideal divergence is 21 degrees. An analysis of the rotation of emitter and receiver components was made. The main conclusion of this analysis is: rotating the emitter increases the optimal divergence, while turning the plane of sensors decreases it. All of these results provide a more exact simulation of underwater wireless optical communications, and we expect the graphs obtained here might be of help in the design of optical underwater wireless systems in AUVs communication scenarios. Also, a machine learning algorithm based on a Random Forest regression was successfully applied to predict the radial offset and angle of the AUV in relation to a fixed sensor scheme based on the received light power distribution of each lens. The maximum root medium square error obtained was of 6mm for the radial offset prediction and 10degrees for the angle, which based on the live conditions are considered good results.

For future work, we suggest the simulation of other lenses schemes with a square disposition for example, and the integrating of the live offset prediction algorithm on a AUV.

Bibliography

[1] Z. Vali, A. Gholami, D. G. Michelson, Z. Ghassemlooy, M. Omoomi, and H. Noori, “Use of gaussian beam divergence to compensate for misalignment of underwater wireless optical communication links,” *IET Optoelectron.*, vol. 11, no. 5, pp. 171–175, Oct. 2017. [Cited on pages 1 and 44.]

[2] W. Cox, “A 1 mbps underwater communication system using a 405 nm laser diode and photomultiplier tube,” 2008. [Cited on page 1.]

[3] J. Simpson, “A 1 mbps underwater communications system using leds and photodiodes with signal processing capability,” 2008. [Cited on page 1.]

[4] G. Schirripa Spagnolo, L. Cozzella, and F. Leccese, “Underwater optical wireless communications: Overview,” *Sensors (Basel)*, vol. 20, no. 8, p. 2261, Apr. 2020. [Cited on pages xi, 2, and 3.]

[5] NewScientist, “Flash that shield,” http://precog.iiitd.edu.in/people/anupama, Aug. 2021. [Cited on page 5.]

[6] C. H. Sterling, *Military communications: from ancient times to the 21st century*. Abc-clio, 2008. [Cited on page 5.]

[7] D. R. McConathy, “Submarine laser communications,” in *EASCON ’82; Annual Electronics and Aerospace Systems Conference*, Jan. 1982, pp. 277–282. [Cited on page 5.]

[8] T. Wiener and S. Karp, “The role of blue/green laser systems in strategic submarine communications,” *IEEE Transactions on Communications*, vol. 28, no. 9, pp. 1602–1607, 1980. [Cited on page 5.]

[9] M. V. Jamali, J. A. Salehi, and F. Akhoundi, “Performance studies of underwater wireless optical communication systems with spatial diversity: Mimo scheme,” *IEEE Transactions on Communications*, vol. 65, no. 3, pp. 1176–1192, 2017. [Cited on page 6.]

[10] A. Shaw, A. Al-Shamma'a, S. Wylie, and D. Toal, "Experimental investigations of electromagnetic wave propagation in seawater," in *2006 European Microwave Conference*, 2006, pp. 572–575. [Cited on page 6.]

[11] M. Lanzagorta, "Underwater communications," *Synthesis lectures on communications*, vol. 5, no. 2, pp. 1–129, 2012. [Cited on pages xi, 6, and 7.]

[12] G. S. Spagnolo, L. Cozzella, and F. Leccese, "Underwater optical wireless communications: Overview," *Sensors*, vol. 20, no. 8, p. 2261, Apr. 2020. [Online]. Available: https://doi.org/10.3390/s20082261 [Cited on page 8.]

[13] H. Kaushal and G. Kaddoum, "Underwater optical wireless communication," *IEEE Access*, vol. 4, pp. 1518–1547, 2016. [Cited on pages xi and 8.]

[14] W. Popoola, E. Guler, J. Wang, and C. Geldard, "Gbps underwater optical wireless communication in turbulence and random sea surface," in *Proceedings of the Workshop on Internet of Lights*. ACM, Jun. 2021. [Online]. Available: https://doi.org/10.1145/3469264.3469804 [Cited on page 9.]

[15] M. Doniec and D. Rus, "Bidirectional optical communication with aquaoptical ii," *2010 IEEE International Conference on Communication Systems*, pp. 390–394, 2010. [Cited on page 9.]

[16] P. Tian, X. Liu, S. Yi, Y. Huang, S. Zhang, X. Zhou, L. Hu, L. Zheng, and R. Liu, "High-speed underwater optical wireless communication using a blue gan-based micro-led," *Opt. Express*, vol. 25, no. 2, pp. 1193–1201, Jan 2017. [Online]. Available: http://www.osapublishing.org/oe/abstract.cfm?URI=oe-25-2-1193 [Cited on page 9.]

[17] H. M. Oubei, J. R. Duran, B. Janjua, H.-Y. Wang, C.-T. Tsai, Y.-C. Chi, T. K. Ng, H.-C. Kuo, J.-H. He, M.-S. Alouini, G.-R. Lin, and B. S. Ooi, "4.8 gbit/s 16-qam-ofdm transmission based on compact 450-nm laser for underwater wireless optical communication," *Opt. Express*, vol. 23, no. 18, pp. 23 302–23 309, Sep 2015. [Online]. Available: http://www.osapublishing.org/oe/abstract.cfm?URI=oe-23-18-23302 [Cited on page 9.]

[18] T.-C. Wu, Y.-C. Chi, H.-Y. Wang, C.-T. Tsai, and G.-R. Lin, "Blue laser diode enables underwater communication at 12.4 gbps," *Scientific Reports*, vol. 7, p. 40480, 01 2017. [Cited on page 9.]

[19] J. Du, Y. Wang, C. Fei, R. Chen, G. Zhang, X. Hong, and S. He, "Experimental demonstration of 50-m/5-gbps underwater optical wireless communication with low-complexity chaotic encryption," *Opt. Express*, vol. 29, no. 2, pp. 783–796, Jan 2021. [Online]. Available: http://www.osapublishing.org/oe/abstract.cfm?URI=oe-29-2-783 [Cited on page 9.]

[20] C. Shen, Y. Guo, H. M. Oubei, T. K. Ng, G. Liu, K.-H. Park, K.-T. Ho, M.-S. Alouini, and B. S. Ooi, "20-meter underwater wireless optical communication link with 1.5 gbps data rate," *Opt. Express*, vol. 24, no. 22, pp. 25 502–25 509, Oct 2016. [Online]. Available: http://www.osapublishing.org/oe/abstract.cfm?URI=oe-24-22-25502 [Cited on page 9.]

[21] X. Liu, S. Yi, X. Zhou, Z. Fang, Z.-J. Qiu, L. Hu, C. Cong, L. Zheng, R. Liu, and P. Tian, "34.5 m underwater optical wireless communication with 2.70 gbps data rate based on a green laser diode with nrz-ook modulation," *Opt. Express*, vol. 25, no. 22, pp. 27 937–27 947, Oct 2017. [Online]. Available: http://www.osapublishing.org/oe/abstract.cfm?URI=oe-25-22-27937 [Cited on page 9.]

[22] H.-H. Lu, C.-Y. Li, H.-H. Lin, W.-S. Tsai, C.-A. Chu, B.-R. Chen, and C.-J. Wu, "An 8 m/9.6 gbps underwater wireless optical communication system," *IEEE Photonics Journal*, vol. 8, 10 2016. [Cited on page 9.]

[23] X. Hong, C. Fei, G. Zhang, and S. He, "Probabilistically shaped 256-qam-ofdm transmission in underwater wireless optical communication system," in *Optical Fiber Communication Conference (OFC) 2019*. Optical Society of America, 2019, p. Th2A.40. [Online]. Available: http://www.osapublishing.org/abstract.cfm?URI=OFC-2019-Th2A.40 [Cited on page 9.]

[24] C. Fei, X. Hong, G. Zhang, J. Du, Y. Gong, J. Evans, and S. He, "16.6 gbps data rate for underwater wireless optical transmission with single laser diode achieved with discrete multi-tone and post nonlinear equalization," *Opt. Express*, vol. 26, no. 26, pp. 34 060–34 069, Dec 2018. [Online]. Available: http://www.osapublishing.org/oe/abstract.cfm?URI=oe-26-26-34060 [Cited on page 9.]

[25] W.-S. Tsai, H.-H. Lu, H.-W. Wu, C.-W. Su, and Y.-C. Huang, "A 30 gb/s PAM4 underwater wireless laser transmission system with optical beam reducer/expander," *Scientific Reports*, vol. 9, no. 1, Jun. 2019. [Online]. Available: https://doi.org/10.1038/s41598-019-45125-y [Cited on page 9.]

[26] M. Kong, Y. Chen, R. Sarwar, B. Sun, Z. Xu, J. Han, J. Chen, H. Qin, and J. Xu, "Underwater wireless optical communication using an arrayed transmitter/receiver and optical superimposition-based pam-4 signal," *Opt. Express*, vol. 26, no. 3, pp. 3087–3097, Feb 2018. [Online]. Available: http://www.osapublishing.org/oe/abstract.cfm?URI=oe-26-3-3087 [Cited on page 9.]

[27] Z. Zeng, S. Fu, H. Zhang, Y. Dong, and J. Cheng, "A survey of underwater optical wireless communications," *IEEE Communications Surveys Tutorials*, vol. 19, no. 1, pp. 204–238, 2017. [Cited on pages xi, 9, and 10.]

[28] L. Narodny, "Qed: The strange theory of light and matter by richard feynman," *Leonardo*, vol. 24, no. 4, pp. 493–494, 1991. [Cited on page 10.]

[29] D. F. Swinehart, "The beer-lambert law," *Journal of Chemical Education*, vol. 39, no. 7, p. 333, Jul. 1962. [Online]. Available: https://doi.org/10.1021/ed039p333 [Cited on pages 10 and 11.]

[30] A. Sassaroli and F. Martelli, "Equivalence of four monte carlo methods for photon migration in turbid media," *J. Opt. Soc. Am. A*, vol. 29, no. 10, pp. 2110–2117, Oct 2012. [Online]. Available: http://www.osapublishing.org/josaa/abstract.cfm?URI=josaa-29-10-2110 [Cited on pages 11, 28, and 41.]

[31] C. D. Mobley and C. D. Mobley, *Light and water: radiative transfer in natural waters*. Academic press, 1994. [Cited on pages 13, 18, 19, 21, and 27.]

[32] Z. Zeng, S. Fu, H. Zhang, Y. Dong, and J. Cheng, "A survey of underwater optical wireless communications," *IEEE Communications Surveys & Tutorials*, vol. 19, no. 1, pp. 204–238, 2017. [Online]. Available: https://doi.org/10.1109/comst.2016.2618841 [Cited on pages xi, 15, 16, and 17.]

[33] R. C. Smith, R. W. Austin, and T. J. Petzold, *Volume-Scattering Functions in Ocean Waters*. Boston, MA: Springer US, 1974, pp. 61–72. [Online]. Available: https://doi.org/10.1007/978-1-4684-8529-5_4 [Cited on pages xi and 20.]

[34] S. K. Sahu and P. Shanmugam, "A study on the effect of scattering properties of marine particles on underwater optical wireless communication channel characteristics," in *OCEANS 2017 - Aberdeen*, 2017, pp. 1–7. [Cited on pages xi, 20, and 21.]

[35] W. Cox, "Simulation, modeling, and design of underwater optical communication systems." 2012. [Cited on pages xi, 23, 24, 25, 29, and 30.]

[36] F. L. Pedrotti, L. M. Pedrotti, and L. S. Pedrotti, *Introduction to optics*. Cambridge University Press, 2017. [Cited on page 25.]

[37] L. Devroye, "Sample-based non-uniform random variate generation," in *Proceedings of the 18th conference on Winter simulation*, 1986, pp. 260–265. [Cited on page 27.]

[38] W. Cox and J. Muth, "Simulating channel losses in an underwater optical communication system," *Journal of the Optical Society of America A*, vol. 31, no. 5, p. 920, Apr. 2014. [Online]. Available: https://doi.org/10.1364/josaa.31.000920 [Cited on page 29.]

[39] T. Möller and J. F. Hughes, "Efficiently building a matrix to rotate one vector to another," *Journal of graphics tools*, vol. 4, no. 4, pp. 1–4, 1999. [Cited on page 30.]

[40] A. S. Glassner, *An introduction to ray tracing*. Morgan Kaufmann, 1989. [Cited on page 33.]

[41] R. L. Graham, B. D. Lubachevsky, K. J. Nurmela, and P. R. Östergård, "Dense packings of congruent circles in a circle," *Discrete Mathematics*, vol. 181, no. 1-3, pp. 139–154, 1998. [Cited on pages 33 and 49.]

[42] M. R. Bonyadi and Z. Michalewicz, "Particle swarm optimization for single objective continuous space problems: A review," *Evolutionary Computation*, vol. 25, no. 1, pp. 1–54, 2017. [Cited on page 37.]

[43] P. E. Utgoff, *Machine Learning*, vol. 4, no. 2, pp. 161–186, 1989. [Online]. Available: https://doi.org/10.1023/a:1022699900025 [Cited on page 38.]

[44] J. H. Friedman, *The elements of statistical learning: Data mining, inference, and prediction*. springer open, 2017. [Cited on page 39.]

[45] "Uv fused silica bi-convex lenses, uv ar coated," https://www.thorlabs.com/newgrouppage9.cfm?objectgroup_id=3540, accessed: 2010-09-30. [Cited on page 43.]